

THERMAL FLUID CIRCULATION AROUND THE KARLIOVA TRIPLE JUNCTION: GEOCHEMICAL FEATURES AND VOLCANO-TECTONIC IMPLICATIONS (EASTERN TURKEY)

Özgür Karaoğlu^{1*}, Mohsen Bazargan^{2,3}, Alper Baba⁴, John Browning⁵

¹Eskişehir Osmangazi University, Department of Geological Engineering, 26040 Eskişehir, Turkey

²Department of Earth Sciences, Royal Holloway University of London, Egham, TW20 0EX, UK

³Department of Research and Development, Weld On Sweden, Vaxjo, Sweden

⁴Izmir Institute of Technology, Engineering Faculty, 35430, Urla, Izmir, Turkey

⁵Department of Mining Engineering and Department of Structural and Geotechnical Engineering, Pontificia Universidad Católica de Chile, Santiago, Chile

* Correspondence to Ö. Karaoğlu, ozgur.karaoglu@deu.edu.tr

Abstract

The Karliova triple junction (KTJ) in eastern Turkey has been subjected to incremental deformation resulting in complex kinematic and mechanical interactions throughout the upper crust. These interactions have generated tectonic inversions and uplift, extensive seismicity and volcanism. The regional tectonics generate local stresses, some of which are favorable to magma transport and thermal water circulation throughout the lithosphere. Here we evaluate hydrogeochemical, geological and numerical results relating to the mechanism of thermal fluid circulation around the KTJ. Hydrogeochemistry of the samples indicates that the thermal water springs are probably heated by steam. Volcanic rocks at the site appear to be the host rock owing to the enrichment of Na⁺ and Cl⁻ ions in water and the abundance of these elements in minerals of the volcanic rocks. In addition, it is clear that the thermal fluids are sourced from depth and migrate through permeable networks of faults. The effects of crustal heterogeneities, in particular the geometry and mechanical properties of many faults and layers, on thermal fluid circulation in relation to active magma chambers were investigated under a variety of different mechanical conditions. The numerical results indicate very close relationships between the stress field causing faulting and thermal fluid movement in the KTJ. Thermal transfer effects were modeled throughout the crust and along the crustal surface. The models show that some faults encourage thermal fluid circulation below the Varto and Özenç volcanoes. Hydrogeochemical, geological and numerical results suggest that magmas residing beneath both the Varto caldera and the Özenç volcano are the main heat source for thermal fluid in the Varto region. Fluid-solid interactions and fluid circulation models show that the permeable faults are important factors affecting heat transport and fluid circulation. In a series of thermal fluid flow models we probe the mechanism for fluid and gas transport from the 900 °C 'hot' zone around the deep magma chambers and how heat is lost throughout the crust on the way to the surface and so eventually creates water channels of temperatures between 50 to 60 °C.

Keywords: Fluid circulation; Thermal water; Karliova triple junction; Caldera; Tectonic

1. Introduction

Faults and fractures which accommodate the deformation of large sections of the upper crust have a significant impact on the physical processes controlling heat transfer and fluid motion in the subsurface. This is because they disturb the conformal succession of geological layers (Press and Siever, 1995). In addition, the mechanical properties of the rocks, the hydraulic characteristics of the rocks, and the geologic and also geodynamic relations provide useful information about thermal fluid circulation through the fractured upper crust. Numerical modeling provides one approach to estimate the structural setting of the subsurface and the mechanical processes controlling fluid and heat transfer (e.g., Cherubini et al., 2013).

The emplacement of hot asthenospheric mantle into shallow levels beneath the crustal materials of the Karlıova-type triple junction could be expected to generate magmatism and possibly thermal water potential. Consistent with this expectation, sequences of volcanic centers have historically erupted along the triple junction within Karlıova (e.g., Furlong and Schwartz, 2004).

Geothermal systems are linked to magmatism in a variety of geodynamic contexts in volcanic environments (i.e., island arcs, hot-spots, middle oceanic ridges, sea-mounts, intraplate volcanism and intrusions) (Caracausi et al., 2005). Thermal fluid circulation is affected by both temporal variations in degassing and in the activity level of the magmatic systems supplying fluids and energy to the geothermal reservoirs (Baker, 1995; Von Damm et al., 1995; Baker and Urabe, 1996; Giggenbach, 1996; Caracausi et al., 2005). Active tectonics and very recent volcanic activity have a strong impact on the geochemistry of the circulating fluids (e.g., Italiano et al. 2013).

A triple junction that deforms the upper crust in a complex manner is a site of special interest in which to study thermal and cold water transportation. Geometric consequences of the motions of three plates, following a collision between convergent plates, mostly result in extrusion through crustal-scale transtensive faults. Triple junction tectonics can produce surface uplift and crustal deformation, abundant seismic activity, high heat flow, and the eruption of volcanoes on the Earth's surface (e.g., Furlong and Schwartz, 2004).

In order to better understand the source and thermo-mechanical constraints on hydrothermal systems, the detailed geologic background and geochemical analysis of the fluids, which in turn form a numerical modeling approach, must first be evaluated. The young Karlıova-Varto volcanic terrain provides an excellent opportunity to explore the relationships between magmatic heat sources (i.e., magma chambers, magma storage, magma plumes, hot spots) and geothermal fluids throughout the upper crust.

The aim of the study is to demonstrate how hydrothermal systems follow paths with different dimensions along these faults, and also how a fluid behaves in this intensely deformed crust. The hydrogeochemistry of geothermal springs around the Varto volcanic province is documented in order to link geochemical constraints with thermo-mechanical controls on fluids in the crust.

2. Tectonic and Geologic setting

Eastern Turkey represents a particular part of the Mediterranean region which is characterized by the presence of major continental fragments and suture zones (e.g., Isik et al., 2014). The closure of the Neotethyan Ocean along the BZSZ during the Cretaceous-early Paleogene led to the formation of the Eastern Anatolian Accretionary Complex (EAAC), which has subsequently acted as one of the major tectonic units during the subsequent tectonic evolution of the region (Barka, 1992; Okay and Tüysüz, 1999; Bozkurt, 2001).

The Karlıova triple junction area is one of the best examples of an active continental collision zone in the world (Fig. 1). The location, timing and geochemical characteristics of volcanism result from the complex interaction of the colliding Eurasian and Afro-Arabian

51 plates. Escape tectonics of the Anatolian plate to the west gave rise to strike-slip motion along
52 the North Anatolian Fault Zone (NAFZ) and East Anatolian Fault Zone (EAFZ) after the
53 closure of the Neotethyan Ocean as a result of Arabia-Eurasian convergence (Barka, 1992;
54 Okay and Tüysüz, 1999; Bozkurt, 2001). The Varto Fault Zone (VFZ) presents a structural
55 continuation of the NAFZ starting from the KTJ (Fig. 2). The VFZ is composed of sets of
56 discontinuous faults with differential kinematics and associated sets of striae (Karaoğlu et al.,
57 2017). The VFZ extends for over 50 km and can be subdivided into six segments (Fig. 1b).
58 Fault planes from the VFZ commonly exhibit multiple sets of striations, highlighting
59 incremental and complex deformation of the KTJ region since ~6 Ma (Karaoğlu et al., 2017).

60 The northernmost segment of the VFZ, called the Tuzla Fault, is mainly a thrust fault
61 (Karaoğlu et al., 2017). The western part of these faults is offset laterally by the EAFZ (Fig.
62 1b). The Varto fault is the most seismically active segment of the VFZ, a N70°W-trending-
63 normal fault that offsets the southern part of the Varto caldera (Fig. 1b) (or the Bingöl caldera;
64 Hubert-Ferrari et al., 2009), and was introduced for the first time by Karaoğlu et al. (2017).
65 Several destructive earthquakes ($M_w = 6.8$) shifting further south took place on the Varto fault
66 in 1966 and on the Leylek Fault ($M_w = 6.2$), and there was also a small earthquake ($M_w \geq 3$)
67 on the Çayçatı Fault (Wallace, 1968; Ambraseys and Zatopek, 1968).

68 The first volcanic activity began with high-silica obsidian flows at Çatak on the EAFZ
69 reflecting the southern branch of the triple junction, and started at 6.06 Ma (Poidevin, 1998).
70 Two composite volcanoes were emplaced in the area at around 3 My ago. The Turnadağ
71 volcano located in the western part of KTJ was formed 2.3-2.8 Ma ago, but the Varto caldera
72 was active 2.6-3.1 Ma ago (Fig. 2) (see Pearce et al., 1990; Hubert-Ferrari et al., 2009 for details
73 about K/Ar whole rock and $^{40}\text{Ar}/^{39}\text{Ar}$ groundmass dating of the rocks). The two volcanic domes
74 are 0.46 Ma and 0.73 Ma old (Hubert-Ferrari et al., 2009, see Fig. 2). Recent tomographic
75 image data shows the presence of active magma reservoirs throughout the crust around the
76 Karlıova region (Salah et al., 2011; Karaoğlu et al., 2018).

77 The Varto and Turnadağ volcanoes exhibit quite similar major or trace element
78 compositions. Volcanic rocks from the two volcanoes are composed of high-K and shoshonitic
79 series rocks including trachy-andesite to rhyolite with a small amount of basaltic trachy-
80 andesite (Buket and Temel, 1998; Hubert-Ferrari et al. 2009).

81 Italiano et al. (2013) stated that the release of volcanic fluids is a common feature along
82 the main active faults in Turkey, however the local geological setting is responsible for the
83 uprising of deep fluids through tectonic discontinuities and the occurrence of shallow processes
84 affecting the original characteristics of the circulating fluids. Moreover, the presence of
85 carbonatic rocks, travertine deposits, metamorphic rocks and old volcanic rocks (Fig. 2)
86 accounts for the different nature of the circulating fluids and different fluid-rock interactions
87 (Italiano et al., 2013). Across the Karlıova-Varto area, a volcano-sedimentary package, around
88 45 m thick, interfingers with the effusive and explosive-type volcanic rocks of the Bingöl group
89 (Fig. 2). The former volcano-sedimentary deposits display a well preserved subaqueous-
90 subaerial transition in a fluvio-lacustrine setting generated after some volcanic eruptions. The
91 deposits are composed of mud-poor sandstone, sand-filled pebbles intercalated with the
92 mudstone, which in turn are exposed in restricted plains dissected by braided rivers in the
93 western part of the Varto caldera (Karaoğlu et al., 2017). Most of these volcanoclastic
94 successions have experienced an intense deformation particularly since 6 Ma. These deposits
95 are overlain by lava stacks and ignimbrite veneers of the Varto group. The Pleistocene
96 lacustrine sediments are mainly composed of marl, limestone, and tuff. Tectonic activity has
97 created a faint deformation within these deposits on the plain near Teknedüzü and Yayıklı
98 villages (Fig. 2). Fault complexity is observed in strongly folded lacustrine sediments at a
99 meter-scale, with nearly horizontal axial planes, whose strikes are scattered around an NNE-
100 SSW direction (Fig. 1b). The youngest effusive and extrusive volcanism conformably overlies

101 these sediments. A massive-type travertine is exposed in the northern part of Karlıova, on a
102 continuation of the EAF to the northeast.

103 3. Fault kinematics

104 KTJ is a key area for understanding the deformation of Neogene volcanoes in eastern
105 Turkey because of their progressive inversion tectonics. Structural analysis suggests that this
106 volcano has undergone incremental tectonic controls in eastern Turkey since the Upper
107 Miocene. [Karaoğlu et al. \(2017\)](#) documented 128-slip data points from 16 locations of two
108 transpressional and transtensional deformational fields which were collected for palaeostress
109 analysis (Fig. 3). The fault surfaces document that inversion tectonics dominated the area when
110 both extensional and transtensional deformational phases progressively reversed over the past 3
111 My ([Karaoğlu et al., 2017](#)). Structural data across the Varto Fault Zone (VFZ), obtained from
112 six faults for which kinematics indicate a range of shortening and extensional deformation for
113 3 Ma (Fig. 3). Many fault surfaces show evidence of reactivation. Particularly, the splays of
114 the VFZ and the other segmented faults have thrust to strike-slip fault components, indicating
115 multiple reactivation events. To establish the surface expressions of the deformation process,
116 we present the kinematic data, which was previously published by [Karaoğlu et al. \(2017\)](#), on
117 each fault segment around the Varto region (Fig. 3). The episodic deformation, which took
118 place at Eryurdu, Tuzlu, Varto, Teknedüzü, Leylekdağ, and Çayçatı faults, dominate the
119 southern part of the Varto Caldera (Fig. 3).
120

121 The Eryurdu Fault terminates the southern flank of the Varto Caldera resulting in fault-
122 related volcanic breccia deposits. This fault is offset by the sinistral strike-slip Geyiksuyu Fault
123 (GF) on the southern margin of the Varto Caldera (Fig. 3). The Eryurdu Fault strikes N85°W-
124 and is around 18 km long with mostly high-angle and oblique-slip segments. This fault displays
125 typical high-angle normal fault slickenlines (Fig. 3). Measurements indicate a well-preserved
126 NNE–SSW-trending extension which formed from deformation of the southern part of the
127 Varto caldera ([Karaoğlu et al., 2017](#)).

128 The Tuzla Fault is reported by [Karaoğlu et al. \(2017\)](#) as an active fault due to recorded
129 seismic activities on this fault (Fig. 3). This fault is a thrust fault with a right-lateral component
130 which extends laterally for over 20 km (Fig. 3). Fault kinematics suggest that it underwent a
131 NW-SE directed compression with a maximum stress axis and that this compression has
132 dominated for circa 6 Ma. The Pliocene deposits have been deformed by Tuzla Fault ([Karaoğlu
133 et al., 2017](#)).

134 The N75°W-striking Varto Fault is composed of three sub-parallel segments which
135 extend for 20 km (Fig. 3). A zone of distributed compression affects Pleistocene lacustrine
136 sediments, which accommodate the deformation between the dextral faults. The easternmost
137 segment of the Varto Fault shows dextral offsets for around 1.5 km in the valleys. Westernmost
138 segments display some releasing step-over structures. Kinematic data for this fault poses
139 oblique-slip normal fault surfaces dipping 55°S and with rakes of 35°E (Fig. 3).

140 The Teknedüzü Fault exhibits typical thrust fault constraints of N75°W-striking in
141 different curved strands. The horsetail shape branches deformed up to 20 km in length of the
142 fault (Fig. 3). This fault is regarded as one of the youngest faults because it cuts Pleistocene
143 lava flows as well as recent lacustrine and alluvial deposits ([Karaoğlu et al., 2017](#)). The
144 Teknedüzü Fault is represented by two main strands of The Leylekdağ and Çaydağ reverse
145 faults, both have minor dextral strike-slip components (Fig. 3). The central part of the
146 Leylekdağ Fault was ruptured by an earthquake (Mw 6.2) 20 August 1966.

147 The Varto region, where the thermal and non-thermal springs are most visible, has been
148 subjected to intense deformation due to those reactivated faults. Fault planes of F9 and F10
149 record a NE–SW-directed contraction associated with a NW–SE extension, whilst a coeval
150 phase of F11 developed under NE–SW extension (Fig. 3; [Karaoğlu et al., 2017](#)).

151 The Çayçatı Fault, which displays thrust fault kinematic morphological constraints,
 152 consists of two main segments. The western segment shows a N70E°-striking thrust component
 153 on a 7-km-long transpressional fault (Fig. 3). Evidence for the earthquake faulting scarps and
 154 related deformation generated by the 1966 earthquake can still be observed in this area. The
 155 kinematic data from F12 indicate that a NW–SE-trending extension is associated with the NE–
 156 SW contraction (Fig. 3; [Karaoğlu et al., 2017](#)).

157 Both extensional and transtensional dominated fault motions have been documented on
 158 the extruded Anatolian block ([Karaoğlu et al., 2017](#)) (Fig. 3). Measurements of stress tensors
 159 on the western part of the KTJ indicate E–W-trending extension which is compatible with the
 160 westward motion of the Anatolian block (Fig. 3). However, measurements from point F14 on
 161 Figure 3 indicate a NE–SW-trending extension ([Karaoğlu et al., 2017](#)), point F13 on Figure 3
 162 indicates a sinistral strike-slip fault motion with at least two phases of movement. Both fault
 163 scarps suggest extensional tectonics along the East Anatolian Fault (Fig. 3) ([Karaoğlu et al.,](#)
 164 [2017](#)).

165 4. Governing equations

166 We present three sets of governing equations used to create models in COMSOL
 167 Multiphysics. They are mass balance, momentum and heat transfer.

168 The momentum and mass balance equations are as follows:

$$169 -\nabla \cdot \eta (\nabla \mathbf{u} + (\nabla \mathbf{u})^T) + \frac{\eta}{k} \mathbf{u} + \nabla p = \mathbf{g} \beta_T (T - T_c) \quad (1)$$

$$170 \nabla \cdot \mathbf{u} = 0 \quad (2)$$

171 where p is pressure, \mathbf{u} is a vector of directional velocities, η is dynamic viscosity, k is
 172 permeability, ρ is fluid density, \mathbf{g} is gravity, β_T is thermal expansion coefficient, T is
 173 temperature from the heat transfer application, and T_c is the initial temperature.

174 A buoyant lifting term links flow and heat:

$$175 \nabla \cdot (-k \nabla T + c_p \rho T \mathbf{u}) = 0 \quad (3)$$

176 where, T is temperature, K_e is effective thermal conductivity of the fluid and solid medium, C_L
 177 is fluid volumetric heat capacity, $C_L = c_p \rho$, c_p is fluid specific heat capacity, and \mathbf{u} is a vector of
 178 directional fluid velocities from the flow application ([Versteeg and Malalasekera, 1995](#)).

179 The heat transport in this paper is described by the heat transport equation:

$$180 (\rho C_p)_{eq} \partial T / \partial t + \rho C_p \mathbf{u} \cdot \nabla = \nabla \cdot (k_{eq} \nabla T) + Q + Q_{geo} \quad (4)$$

181 Heat is balanced generally and it is transported by both conduction and convection processes
 182 within a fault zone. Heat can be generated or lost, which can be defined in the source term, Q
 183 . One special feature of heat transfer at the porous medium interface is the hydrothermal

184 heating feature implemented, represented as a domain condition: Q_{geo} . It is also possible to
 185 implement an average representation of rock thermal parameters, comprising the rock structure
 186 and the underground water using the matrix volume fraction, Θ , as a weighting factor (for
 187 further details see the COMSOL website, www.comsol.com).

188 In the case of volume averaging, the volumetric heat capacity in the heat transport equation
 189 becomes:

$$190 (\rho C_p)_{eq} = \sum_i (\theta_{pi} p_{pi} C_{p,pi}) + (1 - \sum_i \theta_{pi}) \rho C_p \quad (5)$$

196 and the thermal conductivity becomes:

$$197 \quad k_{eq} = \sum_i (\theta_{pi} k_{pi}) + (1 - \sum_i \theta_{pi}) \rho C_p \quad (6)$$

198
199 Solving the heat transport properly generally requires incorporation of a flow field. There are
200 various situations in the subsurface which require different approaches to describe the fluid
201 flow mathematically (Durbin, 1986). In this paper we focus on the macro-scale and also take
202 into consideration resolution of flow in pores. However, fully-saturated and mainly pressure-
203 driven flow in deep geothermal strata are sufficiently described by Darcy's law:

$$204 \quad u = -\frac{k}{\mu} \nabla p \quad (7)$$

205
206 where the velocity field, u , depends on the permeability, κ , the fluid's dynamic viscosity, μ
207 and is driven by a pressure gradient, P . Darcy's law is then combined with the continuity
208 equation:

$$209 \quad \frac{\partial}{\partial t} (p \varepsilon_p) + \nabla \cdot (p u) = Q_m \quad (8)$$

210
211 as our scenario concerns geothermal time scales, the time dependence is due to storage effects
212 on the flow and heat transfer from the fluid to solid and vice versa. Therefore, the first term on

213 the left-hand side of the equation above vanishes because the density, ρ , and the porosity, ε_p ,
214 can be assumed to be constant. Usually, the temperature dependencies of the hydraulic
215 properties are also negligible. In some of our models, especially if the number of degrees of
216 freedom is large, it can make sense to utilize independence by splitting the problem into a few
217 time dependant and stationary sections for solution. In the following models, heat transfer from
218 the fluid into solids is only due to conduction (Taler and Duda, 2006). Fourier's law also
219 describes how to define the conductive heat flux, q . This shall be proportional to the
220 temperature gradient:

$$221 \quad q = -k \nabla T \quad (9)$$

$$222 \quad (\rho C_p)_{eq} \frac{\partial T}{\partial t} = \nabla \cdot (k_{eq} \nabla T) + Q \quad (10)$$

223

224 5. Methods

225 5.1. Field investigations

226 To explore the thermo-mechanical relationships of the fault activity, hydrogeology,
227 thermal and fluid circulation we carried out an extensive field study around the Varto-Karlöva
228 region (Fig. 1b). The sampling strategy was developed based on the geological map, cross
229 sections, and also fault surfaces.

230 The sampling study was performed on five hot fluids and two mineral water springs,
231 together with cold waters in November 2008 in the region shown in Fig. 1b. During the field
232 surveys, some physical parameters of water, including pH, electrical conductivity (EC as
233 $\mu\text{S/cm}$), temperature (T as $^\circ\text{C}$), redox potential (Eh as mV) and flow rate (Q as L/s), were
234 measured in-situ with a WTW Multi 340i/SETS. For water-quality monitoring, four sets of
235 samples were collected from each point: a 500 mL sample for major anions and cations; a 1000
236 mL sample for tritium isotopes; a 100 mL sample for oxygen-18 (^{18}O) and deuterium (^2H), and
237 a 100 mL sample for heavy metals and trace elements. To prevent the complex formation of

238 trace elements with oxygen, samples were filtered with 0.45 μ m filter paper, transferred to 50-
239 mL polyethylene bottles and stored at 4 °C.

240

241 5.2. Analytical Methods

242 The heavy metals and trace elements were acidified to pH<2 conditions by adding 0.5
243 ml HNO₃ to prevent the complex formation of trace elements with oxygen and then analyzed
244 by inductively coupled plasma–mass spectroscopy (ICP-MS) at the ACME Laboratories in
245 Canada. Chlorine and HCO₃⁻ were determined volumetrically and SO₄²⁻ by a
246 gravimetric method in the Hacettepe University in Ankara, Turkey.

247 The concentrations of $\delta^2\text{H}$, $\delta^3\text{H}$ and $\delta^{18}\text{O}$ isotopes in water samples were determined
248 in the isotope laboratories of the Hacettepe University in Ankara, Turkey. The analysis was
249 carried out in accordance with the standards defined by the International Atomic Energy
250 Agency (Attendorf and Bowen, 1997). $\delta^{18}\text{O}$ and $\delta^2\text{H}$ analyses were conducted using an MS
251 technique that had an uncertainty of $\pm 0.05\%$ and $\pm 1.0\%$, respectively. These values are
252 expressed conventionally in delta notation as a per-mil deviation from the V-SMOW (Vienna
253 Standard Mean Ocean Water) (Verhagen et al., 1991). Tritium ($\delta^3\text{H}$) analysis was conducted
254 with a liquid scintillation counter after electrolytic enrichment of the water samples with an
255 error of ± 0.8 tritium units (TU) (Attendorf and Bowen, 1997).

256 The data handling was performed by the descriptive manner of specifying water types
257 (facies), their origins and average reservoir (host) rock temperature calculation. Piper and
258 Schoeller diagrams are used to emphasize differences and similarities in terms of water types.
259 Isotope signatures of samples indicate their origins. Solute geothermometer equations were
260 applied to calculate average reservoir rock temperatures.

261

262 5.3. Hydrogeochemical properties of water resources

263 The preliminary evaluation of geological conditions at the site provides some
264 information regarding depths of water circulation, bearing potential of the rocks and their
265 influence on spring water chemistry. To represent the chemistry of the site, twenty water points
266 were sampled, including five hot water springs, two mineral water springs, and twelve spring
267 water and surface water (cold water) (Fig. 1b).

268 The average discharge of thermal springs ranges from 1 to 5 L/sec in the study area
269 (Fig. 1b) (Table 1). Surface temperatures of these springs range from 22.5 to 32 °C, with
270 electrical conductivity (EC) values from 2100 to 5775 $\mu\text{S}/\text{cm}$. The average discharges of
271 mineral waters at that site are between 0.5 and 2 L/sec. Surface temperatures were measured
272 as 13.2 and 14.8 °C. Their electrical conductivity values are also in the range of 719-751 $\mu\text{S}/\text{cm}$.
273 The average discharges of cold water springs in the study area are between 1 and 150 L/sec.
274 Surface temperatures of these springs vary between 4.9 and 11.7 °C and electrical conductivity
275 values range from 51 to 199 $\mu\text{S}/\text{cm}$. Regarding pH values, water samples belonging to the site
276 are entirely in the pH range of ~ 5.4 - ~ 6.2 for hot and mineral waters, and ~ 6.2 - ~ 7.7 for cold
277 waters. Thermal springs have acid character, whereas pH values for cold water springs change
278 from slightly acid, neutral to slightly basic. The ranges of physical parameters measured are
279 affected by outcropping rocks and structural features of the site allow different circulation
280 depths.

281 Volcanic and sedimentary rocks outcrop in the vicinity of the study area and the
282 groundwater flow in the volcanic rocks appears to be controlled by the presence of structural
283 features. The information indicating the circulation depth only arises from alignments of the
284 springs. Thermal, mineral and cold water springs discharge from rocks of Upper Miocene and
285 Upper Pliocene age (Yolüstü Formation of Upper Pliocene, Kohkale Lava and Zırnak
286 Formation of Upper Miocene in Fig. 2).

287 These rocks include both volcanic rocks and intercalated volcanic rocks with
288 continental deposits such as sandstone; therefore, they are water-bearing formations. In
289 addition to this, the NAF in Upper Miocene rocks which can outcrop in the study area controls
290 groundwater transport (see Fig. 1b). Shallow and deep flow paths for the groundwater are
291 reflected in the chemistry of the springs (Table 2). The deep flow paths of groundwater
292 resources consist of more ions than the shallow flow groundwater paths.

293 On the basis of major ion chemistry, the Piper and Schoeller diagrams for the study area
294 are shown in Fig. 4. Both diagrams give not only information about different water types at the
295 site but also their evolution. According to the Schoeller diagram, cold waters can be
296 distinguished easily with low major cations and chloride when compared with geothermal and
297 mineral waters. According to the Piper diagram and water type classification (Deutsch and
298 Siegel, 1997), thermal springs are of Na-HCO₃-Cl and Mg-Na-HCO₃ types; while mineral and
299 cold waters are of Ca-HCO₃ type. To compare the thermal waters with mineral and cold waters,
300 a Cl-SO₄-HCO₃ a ternary plot was used (Fig. 5). This diagram covers the entire spectrum of
301 naturally occurring waters from virtually pure chloride, over mixed chloride-sulfate, to
302 bicarbonate (Giggenbach, 1988; Nicholson, 1993). For the hydrogeochemical data, relative
303 portions of Cl-SO₄-HCO₃ cluster into steam-condensates and dilute Cl-HCO₃ sectors (Fig. 5);
304 see the data labeled 2. According to the scatter diagram each thermal fluid has different
305 concentration of SO₄²⁻ ions (Fig. 6). Sample 2 has a high SO₄²⁻ concentration which comes from
306 volcanic units.

307 The hydrogeochemical facies map of the area is shown in Fig. 7. As seen in Fig. 7, the
308 lower altitudes contain geothermal waters and the zone of Na-HCO₃-Cl. Cold waters discharge
309 at higher altitudes and they represent the zone of Ca-HCO₃.

310 When taking account of the linear arrangement of plotted data in Fig. 4 and the
311 processes of steam condensates and dilution with chloride acting upon them, water types
312 change from dominant Ca²⁺ and HCO₃⁻ ions to dominant Na⁺ and Cl⁻ ions as expressed in Eq.
313 11.



315 Na⁺ and Cl⁻ ions are obtained from the altered volcanic rocks. Consequently, volcanic
316 rocks at the site appear to be the likely host rock owing to enrichment of Na⁺ and Cl⁻ ions in
317 the water and abundance of those elements in minerals in the volcanic rocks. In addition, it is
318 clear that thermal waters have relatively deeper circulation routes than cold water under the
319 assumption that they are fluids ascending due to deep processes (water-rock interaction,
320 boiling, and steam heating; see Nicholson, 1993 for details) which do not affect their isotope
321 compositions and originate in descending cold waters.

322 5.3.1. Isotope Composition of Water Samples

323 $\delta^{18}\text{O}$ (‰) and $\delta^2\text{H}$ (‰) composition of the selected samples is essential to explore
324 whether or not they are meteoric or processed waters. Craig (1961) demonstrated that the $\delta^{18}\text{O}$
325 (‰) and $\delta^2\text{H}$ (‰) ratios of meteoric waters (precipitation, river and lake samples from various
326 countries) fit to a line known as the global meteoric water line (GMWL) represented by the
327 formula in Eq.12.

$$328 \delta\text{D} = 8\delta^{18}\text{O} + 10 \quad (12)$$

329 However, $\delta^{18}\text{O}$ and δD values at any locality are strongly dependent upon distance from
330 the ocean (continental effect), latitude and altitude (Nicholson, 1993). Thereby, regional
331 (RMWL) and especially local meteoric water lines (LMWL) are convenient references for
332 understanding local groundwater isotope variations with reference to local meteoric waters
333 (Mazor, 2004). Isotope signatures of groundwater can shift from meteoric water lines to
334 schematic trends designating processes; each process represents a shift in isotopic composition
335
336

337 to the extent that $\delta^2\text{H}$ as well as $\delta^{18}\text{O}$ enriched. Isotope processes can be separated as surficial
 338 and deep processes including surface evaporation for the former; and water-rock interaction,
 339 steam heating and boiling for the latter respectively. Groundwater influenced by these
 340 processes is defined as processed water mentioned in the first line of this section. To explore
 341 whether the selected samples are processed or not, selected RMWLs (Gat, 1983; Eisenlohr,
 342 1995) and LMWLs (Sayın and Eyüpoğlu, 2005) are used (Eq. 13) and the site data given in
 343 Table 3 are plotted (Fig. 8).

$$\begin{aligned}
 344 \quad \delta\text{D} &= 8\delta^{18}\text{O} + 22.00 \text{ (Eastern Mediterranean)} \\
 345 \quad \delta\text{D} &= 8\delta^{18}\text{O} + 16.00 \text{ (Marmara)} \\
 346 \quad \delta\text{D} &= 8\delta^{18}\text{O} + 10.00 \text{ (Global \& Central Anatolia)} \\
 347 \quad \delta\text{D} &= 8\delta^{18}\text{O} + 11.36 \text{ (Dalbahçe-Erzurum)} \\
 348 \quad \delta\text{D} &= 8\delta^{18}\text{O} + 14.87 \text{ (Şenyurt-Erzurum)}
 \end{aligned}
 \tag{13}$$

351 The data are separated as thermal and cold waters in the diagram and clustered between
 352 the RMWL of Eastern Mediterranean and Marmara. Isotope signatures of the site data do not
 353 show any trend indicating processes.

354 The activity of $\delta^3\text{H}$ indicates groundwater circulation time consumed from recharge to
 355 discharge and can be simply stated that as the lower the $\delta^3\text{H}$ activity in groundwater, the older
 356 it is or it has taken a longer route. This statement is applicable under the assumption of the
 357 piston flow model (no dispersion or mixing between different aged flow paths; see Kazemi et
 358 al., 2006 for details). In this model, the passage of time through which the activity of ^3H
 359 decreases can be calculated by the decay law in Eq. 14 (Kresic, 2007).

$$360 \quad {}^3\text{H}_s = {}^3\text{H}_0 e^{-\lambda t}
 \tag{14}$$

361 where ${}^3\text{H}_s$ is the amount of ^3H in the sample, ${}^3\text{H}_0$ is the activity of ^3H in precipitation, and λ is the
 362 decay constant of tritium of 0.056 year^{-1} . In this equation, the most important point is to
 363 determine the $\delta^3\text{H}$ activity in precipitation, essentially needed for the use of $\delta^3\text{H}$ as a tracer of
 364 groundwater circulation time. Therefore, the activity of $\delta^3\text{H}$ atoms in precipitation water should
 365 be measured to determine peak values of natural $\delta^3\text{H}$ activity. These types of measurements
 366 are related to thermonuclear testing begun in 1952 (Kazemi et al., 2006). During the tests, large
 367 quantities of tritium were released into the atmosphere; hence, natural $\delta^3\text{H}$ in precipitation
 368 between 5 and 20 tritium units (TU) stated by Kaufmann and Libby (1954) reached up to
 369 several thousand TU in precipitation (Mazor, 2004). To sum up, in the year 1952 the start of
 370 thermonuclear tests provided an indicator to determine pre and post-1952 recharge entering
 371 into aquifers. To estimate pre and post-1952 recharge at the site, $\delta^3\text{H}$ values in Table 3 are used.

372 The results indicate that $\delta^3\text{H}$ values lower than 6 TU indicate mixing of pre and post-
 373 1952 recharges, whereas values higher than 6 TU are a sign of post-1952 recharge. Except for
 374 the spring labeled 1 which indicates cold water (post-1952), all thermal waters are mixed with
 375 cold waters. In conclusion, although thermal water samples cluster in steam-
 376 heated/condensates and dilute Cl-HCO_3 sectors on the $\text{Cl-SO}_4\text{-HCO}_3$ ternary plot (Fig. 9) they
 377 do not shift from meteoric water lines. Therefore, steam-heated conditions are available for the
 378 site but for robust checking, solute geothermometers were used. It was expected that the host
 379 rock temperature is lower than that at steam condensate conditions.

382 383 5.3.2. Application of geothermometers to the site data

384 Chemical analyses of geothermal fluids can be used to estimate subsurface reservoir
 385 temperature. The results are given in Table 4. For robust checking, appropriate solution
 386 geothermometers given are explained by providing Giggenbach (1988) and SI diagrams (Reed

387 and Spycher, 1984). The ternary plot of Na/1000–K/100–Mg^{1/2} of Giggenbach (1988) is a
388 method to discriminate mature waters which have attained equilibrium with relevant
389 hydrothermal minerals from immature waters and waters affected by mixing and/or re-
390 equilibration at low temperatures during their circulation (Fig. 9). All samples plotted in the
391 immature water zone in Fig. 9. Reservoir temperature values estimated by this method are
392 invalid because thermal waters mix with some proportions of both cold and mineral waters.
393 Na-K geothermometers thus provide unacceptable results for groundwater samples from this
394 site.

395 A different approach to geothermometry (Reed and Spycher, 1984) is illustrated in Fig.
396 10, where SI (Saturation Indices) are computed as a function of temperature. In the calculation
397 of the mineral saturation indices, the PhreeqC code (Parkhurst and Appelo, 1999) was used. It
398 is easy to note that thermal waters are saturated with respect to dolomite, calcite and aragonite
399 between 50 °C and 80 °C, thus suggesting this range of temperature as reliable for the deep
400 geothermal reservoir temperature (Baba et al., 2010).

401

402 5. 4. Thermal numerical modeling setup

403 In order to investigate magma heat transfer and fluid circulation a series of models is
404 created that replicate the heat from a crustal shallow magma chamber which is overlain by a
405 series of faults. The geometry of the models is based, as closely as possible, on the geology of
406 the region. The various mechanical properties that are input into the models are investigated to
407 obtain the most realistic outputs in terms of surface water temperatures. In the first set of
408 models, shown in Figure 11, vertical fault zones are simulated, each with a different
409 permeability (k). The fault connects a magma chamber with an internal temperature of 900 °C
410 to the surface, the geometry of the magma chamber is not generated and so we simply assign a
411 ‘hot’ boundary. The surface temperature in this model is defined as with atmospheric
412 conditions and so is 25 °C. The bottom of the model is defined with magma chamber conditions
413 and so the given pressure and temperature conditions in this area are 10 MPa and 900 °C
414 respectively, based on an intermediate magma composition (Murase and McBirney, 1973). The
415 lower boundary is fixed, and both the left and right boundaries have no additional load but they
416 are allowed to deform. The upper boundary is a free surface (a region free from shear stress).
417 We present four models of this type (Figs. 11 a,b,c and d) to show the effect of permeability
418 which varies across a narrow range (from 1×10^{-15} in part a to 4.3×10^{-15} in part d) of fluid
419 velocities. Fluid rises in this model as we impose a temperature gradient of 25 °C / km. As such
420 the body temperature in the model varies over distance according to the equation $T = (D.x) +$
421 25.

422 In Figure 12 we extend the results from Figure 11 to investigate the effects of both fault
423 width and fault permeability on heat transfer within the fault. In total we present 18 models,
424 with six different permeabilities ($1.0 \times 10^{-15} \text{ m}^2 - 4.3 \times 10^{-15} \text{ m}^2$) and three different fault widths
425 (1m, 5m and 10 m). The models are designed with permeability steps of $0.1 \times 10^{-15} \text{ m}^2$ and fault
426 width steps of 0.1 m between the minimum and maximum ranges. In total, 430 different
427 permeabilities over 100 different fault widths were investigated, here we present 18
428 representative model results from the full suite of model runs. We run the models to obtain a
429 surface temperature of around 50 °C so as to compare with the field results.

430 In Figure 13 we present a series of linear elastic stress models. These models consider
431 the effects of regional tectonic loading on the fault zones of the KTJ. We imported a surface
432 plan view of the faults from geological maps (Karaoğlu et al., 2016) (Fig 12a), and then
433 assigned a boundary horizontal extension (Fig. 13b) or compression (Fig. 13c) of 5 MPa. The
434 resulting models (Figs 13b and 13c) show the concentration and linkage of tensile stresses
435 around the faults.

436 In the next set of models (Figs 14-15) we use the results from the baseline models
437 presented in Figures 11-12 and combine these with the geological setting of the Karlioiva region
438 (Fig 13). The faults in plan view (Fig 13) are extrapolated throughout the crust based on a
439 constant dip, and interactions are inferred (Karaoğlu et al., 2016). The boundary conditions in
440 Figure 15 are fixed with a constraint on the horizontal edges, a set pressure and temperature on
441 the lower boundary and a free surface on the upper boundary. The deepest fault inferred is
442 around 10 kilometers, and so we set a pressure gradient of 10 MPa/km, and a temperature
443 gradient of 25°C/km. A porous medium with a very low permeability was defined as the host
444 rock in order to prevent fluid leakage from the fault to the host rock. The system cannot model
445 fluid losses and so heat transfer takes place only from the fluid to the solid. This happens while
446 the fluid is passing within the fault as the model edges are fixed for any Y direction movements.
447 For this reason, this model will not be affected by the fault zone to the right or left side of the
448 model or by any effect from these two sides of the medium.

449 In Figure 15, we plot the fluid velocity field in several orientations although the fracture
450 network that creates the permeability is assumed to be isotropic. This is a limitation that we
451 seek to investigate further in the future as it is well known that fault zones in complex tectonic
452 regimes may be overprinted with anisotropic fracture networks (e.g., Browning et al., 2018).

453

454 **6. Results**

455 *6.1 Fluid and solid interactions*

456 In order to better understand fluid and heat transport throughout crustal structures such
457 as permeable faults, we created models to investigate the effects of fluid and heat transfer (Figs.
458 11 and 12). In Figure 11 we show how fluid velocity changes within the fault zones as a
459 function of permeability. These models represent fluid at pressures of 10 MPa injected into the
460 fault (Fig. 11). The fault zone has a fixed size but the permeability varies by a factor of four.
461 Permeability values are $1 \times 10^{-15} \text{m}^2$ to $4.3 \times 10^{-15} \text{m}^2$. In all the models the fastest velocities are
462 found in the centre of the fault (assuming a homogenous fracture network), simulating a
463 Poiseuille like flow. In the faults with the lowest permeabilities (Figs. 11a and 11b) the initial
464 fluid velocity decreases almost immediately after fluid injection and is sustained for a
465 maximum of 40% of the fault length. However, when the permeability is increased (even if
466 only by a factor of 4) the initial injection fluid velocity is sustained for almost the entire length
467 of the fault (Figs. 11c and Fig. 11d).

468 The rate at which fluids can pass through the fault network obviously has implications
469 for how quickly heat within the fluid and/or gas is transferred to the surrounding rocks.
470 Essentially when a fluid or a gas is flowing with a high velocity, there will be less interactions
471 with the rock body so less heat is transferred to the porous medium. In Figure 12 we consider
472 this problem by presenting models that investigate how the temperature of the fluid with an
473 initial magma temperature of 900 °C interacts with the body (crustal rocks) while it moves
474 vertically through the fault to the surface (Fig. 12). Over the 10 km of the fault the fluid loses
475 almost all its heat, around 875 °C depending on the permeability of the fault. We find, in all
476 cases, that fault width has little effect in changing the temperature distribution. It is clear that
477 the hot zone in part A5 (Fig. 12) is 4 times higher than A1 (Fig. 12). In A1 (Fig. 12), the
478 temperature decreases rapidly to 700 °C (within a few tens of metres). In Figure 12, part A6,
479 the fluid remains with a temperature of 900 °C for almost 50% of the fault length. The body
480 (crust) of the model medium uses the elastic parameters of Young Modulus (E) 40 GPa,
481 Poisson's ratio 0.25 and a density of 3300 Kg/m². The fluid thermal conductivity is
482 $6[\text{W}/(\text{m} \cdot \text{K})]$, the fluid ratio of specific heat is 1, and the fluid heat capacity at constant pressure
483 is $4200[\text{J}/(\text{kg} \cdot \text{K})]$. The heat transfer coefficient, heat convection and heat conduction will all
484 affect the fluid flow in the fault.

485 Both these models show that the properties of the material within the fault and their
486 respective damage characteristics have significant effects on controlling the movement of both
487 fluid and heat.

488

489 *6.2. Stress intensity around the Karlova triple junction*

490 In order to better understand the mechanical relations between stress intensity and
491 thermal fluid discharge to the surface, a series of stress models were created (Fig. 13). These
492 models are very important in terms of identifying the location of thermal fluid outflow points
493 as tensile stress intensity may indicate areas of fracture and fault dilation and hence increased
494 permeability. The stress concentration models show that the main faults (e.g. NAF, EAF and
495 VFZ) are zones of maximum stress concentration and are thereby likely to control the majority
496 of fluid flow within the region (Fig. 13). During periods of regional extension associated to
497 extrusion of the Anatolian plate we find that the main result is that a NE-SW strike is dominant
498 for the main crustal strain deformation (e.g., Karaoğlu et al., 2017, Figs. 3 and 13b). During
499 periods of regional compression we find a N-S compressional deformation is the main driving
500 deformation process in the Karlova Triple Junction (e.g., Karaoğlu et al., 2017, Figs. 3 and
501 13c).

502

503 *6.3. Fluid circulation models in the KTJ*

504 To investigate fluid circulation throughout the upper crust for the specific case of the
505 KTJ, some additional models were developed (based on heat transfer and velocity considering
506 the geological setting around the KTJ, Figs. 14 and 15). In this model, velocity changes were
507 observed in the fault zone based on permeability changes. The velocity changes in each fault
508 show how it is possible to have fluid flowing inside that fault. It is very important to determine
509 why hot fluid concentrates in some areas and not in others. Rivers are fed by both hot and cold
510 waters sourced from underground but the situation is even more complex as some of the rivers
511 are relatively close to each other. This is one of the challenges that we attempt to deal with
512 using geomechanical rationale which highlights why both hot and cold fluids can form over
513 very narrow areas (Fig. 2). The origin of hot waters can then be discussed but for this discussion
514 it is necessary to return and use model setups from the model series A-C (A1-6) (Figure 12).

515 In Figure 15 we present the pressure changes within the faults (Fig. 15 A1-B1), the
516 resulting fluid velocities (Fig. 15 A2-B4), and the temperature field (Fig. 15 A5-B5). In Fig 15
517 A1-B1 we note that pressure concentrations around the faults increase from this deformative
518 fault zone at outer province. This pressure value reaches to 6 MPa through the upper crust
519 where the western part of the KTJ is (Fig. 13 A1-B1). The minimum pressure value of 1 MPa
520 (maximum) is characteristic for the fault zone (Fig. 13 A1-B1).

521 In Figs. 15 A2-B4 we compare the effects of different permability values on fluid
522 velocity. The main finding is that increasing the permeability increases the fluid velocity at
523 faults (Figs. 15 B2-B4). Applying a value of the $4.3 \times 10^{-15} \text{ m}^2$ rather than $1 \times 10^{-15} \text{ m}^2$, which
524 is in the total velocity field, clearly demonstrates the the effect of the fluid velocity within these
525 faults. We note that a fault placed at the eastern side of the section show a value from 5.0 to
526 $5.6 \times 10^3 \text{ } \mu\text{m/s}$ (Fig. 15 A2-B2). Such an effect can be observed in all faults (Figs. 15 A2-B2).
527 In Figs 15 A3-B5 in the E-W profile we apply vertical and horizontal fluid velocity cases. We
528 note again that there is a substantial incremental change between vertical (Figs. 15 A3-B3) and
529 horizontal cases (Fig. 15 A4-B4). While this fluid velocity value is around $5.4 \times 10^3 \text{ } \mu\text{m/s}$ (Fig.
530 15 B3), the values around $4.4 \times 10^3 \text{ } \mu\text{m/s}$ (Fig. 15 B4).

531 Our numerical model indicate that the temperature field show a markedly greater values
532 around the fault zone (Figs. 15 A5-B5). These value reach to 900 °C particularly in the deeper
533 zone, whilst the temperature show a decrease (between 100-300 °C) where the cross faults

534 interact to each other (Figs. 15 A5-B5). We note that there is no substantial effect of the
535 changing of permeability values on temperature field (Figs. 15 A5-B5).

536 In this model, it can be observed that pressure is relatively constant at different
537 permeabilities and so the temperature does not change dramatically. The temperature inside the
538 fault zone changes similar to the model in Fig. 15 (A5 and B5). The model also displays how
539 permeability in the fault zone affects fluid circulation, while there is no substantial impact on
540 the solid porous matrix.

541

542 **7. Discussion and Conclusions**

543 Kinematic data is a very useful tool to better understand the episodic deformational
544 fields and fluid circulation interactions throughout the crust underneath the KTJ region (Fig.
545 3). Field studies coordinated with kinematic data show that the complexity of these fault
546 deformations indicate variations in the local stress field following initial activity of a westward
547 extrusion of the Anatolian plate since 6 Ma. The direction of the compressive principal stress
548 (σ_1) has been shifted during this deformational period. This direction and local stress fields
549 imply major controls of both magmatic fluids on magma propagation as an individual volcano,
550 or fluid circulation throughout the crust in the region (Fig. 3).

551 Since Late Miocene, deformation of the KTJ has been controlled by the combined
552 effects of continuing compressional tectonics due to a regional shortening of Eastern Anatolia.
553 This shortening is represented by a local stress field, and the westward displacement of
554 Anatolia, which has kinematically responded through a local extensional stress field and
555 coincides with transtensional tectonics (Fig. 3). In this framework, a successive and reactive
556 tectonic motion has caused the incremental complex movement of numerous fault blocks which
557 have resulted in mostly non-thermal but rarely thermal fluid circulation within intensely-
558 deformed crustal materials. This is illustrated by the local stress fields and thermal and non-
559 thermal spring points (Fig. 3). We note that non-thermal fluids are likely concentrated around
560 zones of high minimum principal compressive (maximum tensile) stress (σ_3) (Fig. 3). Although
561 these zones are expected as sources for thermal waters, the non-thermal waters like thermal
562 waters tend to also circulate within the upper crust. These non-thermal waters may therefore
563 be circulating in open fractures and faults in the upper level of the crust, but have not yet been
564 subject to heating processes. Thus, these non-thermal waters may be temporally younger than
565 other thermal water sources.

566 The fault stations of F3, 5, 8, 11, 15 and 16 show that an extensional regime agrees
567 well with the location of non-thermal waters (Fig. 3). However, both non-thermal and thermal
568 waters are found to circulate not only in extensional but also in compressional regimes (Fig.
569 3). So, the combined field and numerical studies show that crustal heterogeneity in the form of
570 faults, as well as fault attitude and mechanical properties of both the crust and crustal faults,
571 below the KTJ encourage fluid circulation in the region.

572 Field data and results from a suite of numerical modeling tests indicate that thermal
573 water transport is influenced by the depth of intruded magmas and the permeability of crustal
574 faults in the upper crust.

575 Magma chamber location plays a prominent role in the surface discharge of hot water
576 around the Varto region (Fig. 1b). The thermal water discharge points are located just between
577 the Varto caldera to the north, and the Özenç volcano to the east (Fig. 2). Numerical models
578 indicate that maximum tensile and shear stresses concentrate at the lateral margins of magma
579 chambers and at the Earth's surface above the magma chamber (see [Karaoğlu et al., 2016](#)).
580 These stress accumulation zones are directly associated with thermal water circulation through
581 the crust (Fig. 13). So, these thermal water locations in the region might be related to this stress
582 intensity and fluid interaction. In volcanoes worldwide, the thermal water cycle might be used
583 to indicate the lateral margins of magma chambers as zones of increased faulting and fracturing.

584 Hydrogeochemistry of the samples indicates that thermal water springs are likely heated
585 by steam. Field studies, hydrogeochemical data and numerical models suggest that the magma
586 systems beneath both the Varto caldera and the Özenç volcanoes are the main heat source for
587 thermal water in the Varto region.

588 The results reveal that most water in the study area comes from the outcropping
589 volcanic rocks in the Varto Region. The rocks demonstrate typical characteristics of water
590 resources which originate in highly fractured volcanic formations where water seeps through
591 cracks and faults and flows to the surface at lower elevations. On the basis of major ion
592 chemistry, the Piper and Schoeller diagrams (Fig. 4) show that the majority of the cold water
593 resources are of the Ca-HCO₃ type and the thermal water of the Na-HCO₃-Cl type. As the
594 fractures allow a deep circulation of groundwater and a dominant Na-Cl component, we infer
595 that the waters have a volcanic origin. However, the hot waters have the same recharge area as
596 the cold waters. Reliable reservoir temperature ranges for hot waters were obtained with Li-
597 Mg and β-Cristobalite geothermometers as 44-66 °C and 54-80 °C, respectively. These values
598 were also checked with Saturation Indices (SI) vs T diagrams. Results of SI vs T diagrams
599 indicate equilibration with calcite and aragonite. The result shows that jointed volcanic rocks
600 are a reservoir for the geothermal system and that the heat source for the geothermal fluid is
601 the magma chamber.

602 Fluid and solid interactions and fluid circulation models show the role of fault
603 permeability on heat loss during fluid circulation. Also Fig. 12 illustrates what happens to fluid
604 heat loss when the fault permeability and fault width changes. The main boundary condition is
605 the constant injection pressure of 10 MPa. As the pressure is constant and dependent on the
606 injecting boundary, fault width has no obvious effect. The permeability ranged from 1×10^{-15} to
607 4.3×10^{-15} m². When the fault permeability increases, heat loss from 900 °C to 50 °C takes place
608 over a longer distance. In Fig. 15, the model is a combination of two previous models. The
609 same effect of changing permeability of the fault was investigated in a porous medium. The
610 model illustrated that increasing permeability from 1×10^{-15} to 4.3×10^{-15} m² can significantly
611 affect the fluid pressure drop. Fluid injected at pressure declines from 10 MPa to atmospheric
612 pressure over a smaller distance when the permeability is very low. The additional physical
613 parameters added to Fig. 15 is the porous medium body temperature, and also the effects of
614 stress and strain on fluid circulation in the porous medium where observed. These effects
615 usually have little or no impact. However, those effects are very substantial and visible near
616 the boundary area of the fault zone and the porous medium. In these models the detailed
617 structural geology and fault zone are presented to illustrate how a relatively small permeability
618 variation from 1×10^{-15} to 4.3×10^{-15} m² can significantly affect fluid circulation in fault zones.
619 The result is important as the permeability of fault zones can be heterogeneous (Mitchell and
620 Faulkner, 2009) and so for a proper understanding of geothermal resources and hot water fluid
621 circulation this must be considered.

622 623 624 **Acknowledgements**

625 This study was supported by funds from Eskisehir Osmangazi Üniversitesi (Project Numbers:
626 201715031 and 201715A215). Özgür Karaoğlu was supported by The Scientific and
627 Technological Research Council of Turkey (TÜBİTAK) International Postdoctoral Research
628 Fellowship Programme. Mohsen Bazargan was supported by Weld On Sweden for European
629 Doctoral research programme. We are grateful to the editor Eva Schill and three anonymous
630 reviewers, for comments which improved this work.

631 632 **References**

633

634 Ambraseys, N., Zatopek, A., 1968. The Varto Ustukran earthquake of 19 August 1966, B.
635 Seismol. Soc. Am. 58, 47–102.

636 Attendorn HG, Bowen R., 1997. Radioactive and stable isotope geology, Chapman and Hall,
637 London, 519 p

638 Armijo, R., Meyer, B., Hubert-Ferrari, A., Barka, A.A., 1999. Propagation of the North
639 Anatolian fault into the Northern Aegean: timing and kinematics. *Geology* 27, 267–
640 270.

641 Baba, A., Yiğitbaş E., Ertekin C., 2010. Hydrogeochemistry of Geothermal Resources of
642 Eastern Part of Turkey: A Case Study, Varto Region, World Geothermal Congress 2010,
643 25-29 April 2010 Bali, Indonesia, pp.1–8

644 Baker, E., 1995. Characteristics of hydrothermal discharge following a magmatic intrusion.
645 *Geol. Soc. (Lond.) Spec. Publ.* 87, 65–76.

646 Baker, E.T., Urabe, T., 1996. Extensive distribution of hydrothermal plumes along the
647 superfast spreading East Pacific Rise, 13 30'–18 40' S. *J. Geophys. Res-Sol. EA*, 101
648 (B4), 8685–8695.

649 Barka, A.A., 1992. The North Anatolian fault zone. *Ann. Tecton.* 6, 164–195.

650 Bozkurt, E., 2001. Neotectonics of Turkey-A Synthesis. *Geodin. Acta* 14, 3–30.

651 Browning, J., Meredith, P.G., Stuart, C., Harland, S., Healy, D., Mitchell, T.M., 2018. A
652 directional crack damage memory effect in Sandstone under true triaxial loading.
653 *Geophys. Res. Lett.* 45, 6878–6886.

654 Buket, E., Temel, A., 1998. Major-element, trace element, and Sr-Nd isotopic geochemistry
655 and genesis of Varto (Muş) volcanic rocks, Eastern Turkey. *J. Volcanol. Geotherm.*
656 *Res.* 85, 405–422.

657 Caracausi, A., Ditta, M., Italiano, F., Longo, M., Nuccio, P. M., Paonita, A., Rizzo, A., 2005.
658 Changes in fluid geochemistry and physico-chemical conditions of geothermal systems
659 caused by magmatic input: The recent abrupt outgassing off the island of Panarea
660 (Aeolian Islands, Italy). *Geochim. Cosmochim. Ac.* 69(12), 3045–3059.

661 Cherubini, C., Giasi, C. I., Pastore, N., 2013. Evidence of non-Darcy flow and non-Fickian
662 transport in fractured media at laboratory scale. *Hydrol. Earth Syst. Sc.* 17(7), 2599–
663 2611.

664 Craig, H., 1961. Isotopic Variations in Meteoric Waters. *Science* 133, 1702–1703.

665 Deutsch, W., Siegel, R., 1997. *Groundwater Geochemistry: Fundamentals and Applications to*
666 *Contamination*, Lewis Publishers, New York.

667 Durbin, A., 1986. On the k - ϵ Stagnation Point Anomaly, *International Journal of Heat and*
668 *Fluid Flow*, 17, 89–90.

669 Eisenlohr, T., 1995. Die Thermalwässer der Armutlu-Halbinsel (NW-Türkei) und deren
670 Beziehung zu Geologie und Aktiver Tektonik, PhD. Dissertation, ETH-Zürich,
671 Nr.11340.

672 Fournier, R.O., 1991. Water geothermometers applied to geothermal energy. In: D'Amore, F.
673 (Ed.), *Application of Geochemistry in Geothermal Reservoir Development*. UNITAR,
674 Rome, Italy, pp. 37–65.

675 Furlong, K.P., Schwartz, S.Y., 2004. Influence of the Mendocino triple junction on the
676 tectonics of coastal California. *Annu. Rev. Earth Planet. Sci.* 32, 403–433.

677 Gat, J.R., 1983. Precipitation, Groundwater and Surface Waters: Control of Climate Parameters
678 on their isotopic composition and their utilisation as palaeo climatological tools.
679 *Proceedings, Palaeoclimates and Palaeowaters: A Collection of Environmental Isotope*
680 *Studies (Proc. Advisory Group Mtg Vienna, 1980)*, IAEA, Vienna, 3–12.

681 Giggenbach, W.F., 1988. Geothermal Solute Equilibria. Derivation of Na-K-Mg-Ca
682 Geoindicators. *Geochim. Cosmochim. Ac.* 52, 2749–2765.

683 Giggenbach, W.F., 1996. Chemical composition of volcanic gases. In Monitoring and
684 mitigation of volcano hazards. Springer Berlin Heidelberg, pp. 221–256.

685 Herece, E., 2008. Atlas of East Anatolian Fault. General Directorate of Mineral Research
686 and Exploration. Special Publication Series, Ankara, Turkey.

687 Hubert-Ferrari, A., King, G., van der Woerd, J., Villa, I., Altunel, E., Armijo, R., 2009. Long-
688 term evolution of the North Anatolian Fault: new constraints from its eastern termination.
689 In Collision and Collapse at the Africa-Arabia-Eurasia Subduction Zone, edited by D.J.J.
690 van Hinsbergen, M.A. Edwards and R. Govers, Geol. Soc. Spec. Publ. 311, 133–154.

691 Isik, V., Uysal, I. T., Caglayan, A., Seyitoglu, G., 2014. The evolution of intraplate fault
692 systems in central Turkey: Structural evidence and Ar-Ar and Rb-Sr age constraints for
693 the Savcili Fault Zone. *Tectonics*, 33 (10), 1875–1899.

694 Italiano, F., Sasmaz, A., Yuce, G., Okan, O.O., 2013. Thermal fluids along the East Anatolian
695 Fault Zone (EAFZ): Geochemical features and relationships with the tectonic
696 setting. *Chem. Geol.* 339, 103–114.

697 Karaoğlu, Ö., Browning, J., Bazargan, M., Gudmundsson, A., 2016. Numerical modelling of
698 triple-junction tectonics at Karlıova, Eastern Turkey, with implications for regional
699 magma transport. *Earth Planet. Sc. Lett.* 452, 152–170.

700 Karaoğlu, Ö., Sağlam-Selçuk, A., Gudmundsson, A., 2017. Tectonic controls on the
701 Karlıova Triple Junction (Turkey): implications for tectonic inversion and the
702 initiation of volcanism. *Tectonophysics* 694, 368–384.

703 Karaoğlu, Ö., Browning, J., Salah, M.K., Elshaafi, A., Gudmundsson, A., 2018. Depths of
704 magma chambers at three volcanic provinces in the Karlıova region of Eastern
705 Turkey. *B.Volcanol.* 80(9), 69.

706 Kaufmann, S., Libby, W.F., 1954. The Natural Distribution of Tritium. *Physical Review*, 93(6),
707 1337–1344.

708 Kazemi, G.A., Lehr, J.H., Perrochet, P., 2006. *Groundwater Age*, Wiley-Interscience, New
709 Jersey, USA.

710 Kharaka, Y.K., Mariner, R.H., 1989. Chemical geothermometers and their application to
711 formation waters from sedimentary basins. In: Naeser, N.D., McCulloh, T.H. (Eds.),
712 *Thermal History of Sedimentary Basins*. Springer-Verlag, New York, NY, USA, pp.
713 99–117.

714 Kresic, N., 2007. *Hydrogeology and Groundwater Modeling*, CRC Press, Taylor & Francis
715 Group, 2nd Edition, USA.

716 Mazor, E., 2004. *Applied Chemical and Isotopic Groundwater Hydrology*, Marcel Dekker, Inc,
717 3rd Edition, New York.

718 Mitchell, T.M., Faulkner, D.R., 2009. The nature and origin of off-fault damage surrounding
719 strike-slip fault zones with a wide range of displacements: A field study from the
720 Atacama fault system, northern Chile. *Journal of Structural Geology* 31.8: 802-816.

721 Nicholson, K., 1993. *Geothermal Fluids Chemistry and Exploration Techniques*, Springer-
722 Verlag, Berlin.

723 Okay, A.I., Tüysüz, O., 1999. Tethyan sutures of northern Turkey. *Geol. Soc. Spec. Publ.* 156,
724 475–515.

725 Özdemir, Y., Karaoğlu, Ö., Tolluoğlu, A.Ü., Güleç, N., 2006. Volcanostratigraphy and
726 petrogenesis of the Nemrut stratovolcano (East Anatolian High Plateau): the most recent
727 post-collisional volcanism in Turkey. *Chem. Geol.* 226 (3), 189–211.

728 Parkhurst, D.L., Appelo, C.A.J., 1999. *User's Guide to PHREEQC (Version 2) –A Computer*
729 *Program for Speciation Batch-reaction, One-dimensional Transport, and Inverse*
730 *Geochemical Calculations*.

731 Pearce, J.A., Bender, J.F., De Long, S.E., Kidd, W.S.F., Low, P.J., Güner, Y., Saroglu, F.,
732 Yilmaz, Y., Moorbath, S., Mitchell, J.G., 1990. Genesis of collision volcanism in Eastern
733 Anatolia, Turkey. *J. Volcanol. Geotherm. Res.* 44, 189–229.

734 Poidevin, J.L., 1998. Provenance studies of obsidian artefacts in Anatolia using the fission track
735 dating method, An overview, in *L’Obsidienne au Proche et Moyen Orient, du Volcan à*
736 *l’Outil*, edited by A. Gourgaud, B. Gratuze, G. Poupeau, J.L. Poidevin and M.C Cauvin,
737 BAR International Series Hadrian Books 738, 105–156.

738 Press, F., Siever, R., 1995. *Allgemeine Geologie*. Spektrum Akademischer Verlag, Heidelberg
739 Berlin, Oxford.

740 Reed, M., Sycher, N., 1984. Calculation of pH and mineral equilibria in hydrothermal waters
741 with application to geothermometry and studies of boiling and dilution. *Geochim.*
742 *Cosmochim. Ac.* 48, 1479–1492.

743 Salah, M.K., Sahin, S., Aydin, U., 2011. Seismic velocity and Poisson’s ratio tomography of
744 the crust beneath east Anatolia. *J. Asian Earth Sci.* 40, 746–761.

745 Sayın, M., Eyüpoğlu, S.Ö., 2005. Determination of the Local Meteoric Water Lines Using
746 Stable Isotope Contents of Precipitation In Turkey (in Turkish), *Proceedings, II. National*
747 *Symposium of Isotopic Methods in Hydrology*, General Directorate of State Hydraulic
748 Works, İzmir, 323–344.

749

750 Taler, J., Duda, P., 2006. *Solving Direct and Inverse Heat Conduction Problems*. Springer.

751 Tarhan, N., 1991. Hınıs–Varto–Karlıova (Erzurum–Muş–Bingöl) Dolayındaki Neojen
752 Volkanitlerinin Jeolojisi ve Petrolojisi. *MTA Dergisi* 113, 1–15 (in Turkish).

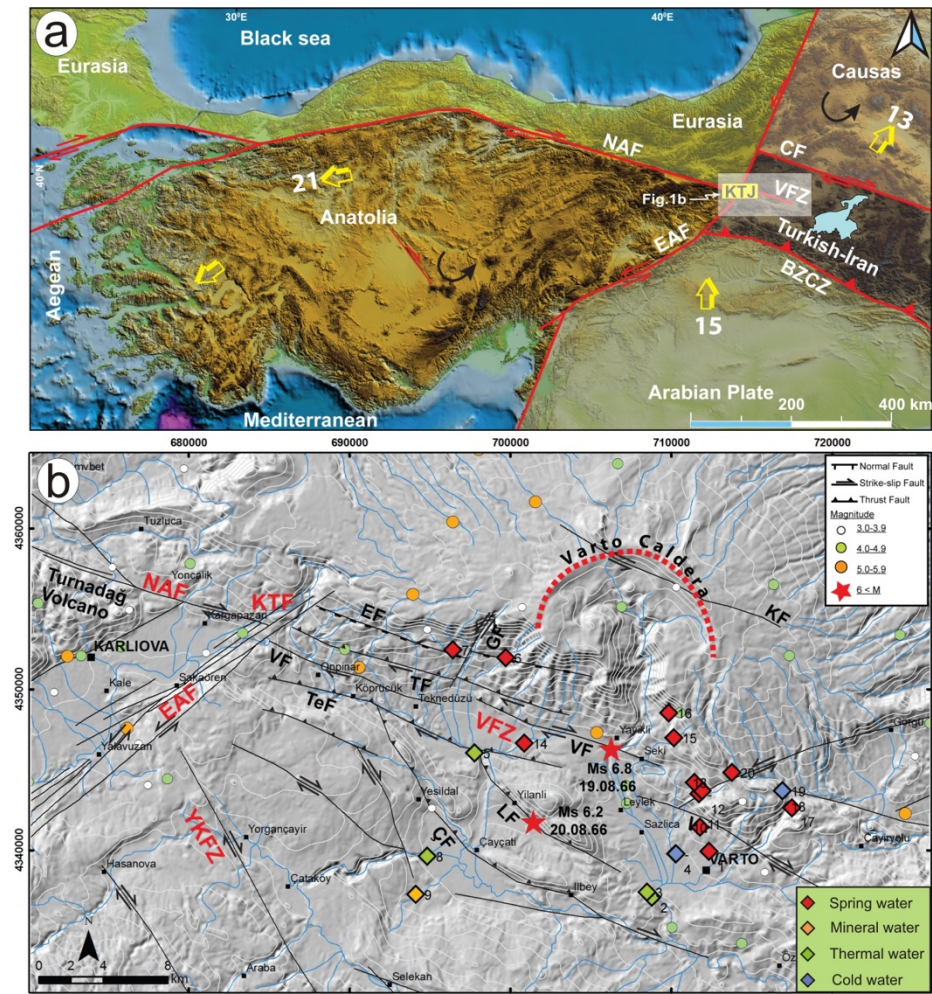
753 Verhagen, B.T., Geyh, M.A., Fröhlich, K. With, K., 1991. Isotope hydrological methods for
754 the quantitative evaluation of groundwater resources in arid and semi-arid
755 areas. *Research Reports of the Federal Ministry for Economic Cooperation of the*
756 *Federal Republic of Germany*, Bonn, Germany, 7–122. Versteeg, H.K., Malalasekera,
757 W., 1995. *An Introduction to Computational Fluid Dynamics*, Prentice Hall, 1995.

758 Wallace, R.E., 1968. Earthquake of August 19, 1966. Varto Area, Eastern Turkey. *B. Seismol.*
759 *Soc. Am.* 58, 11–45.

760
761
762
763
764
765
766
767
768
769
770
771
772
773
774
775
776
777
778
779
780
781
782
783
784

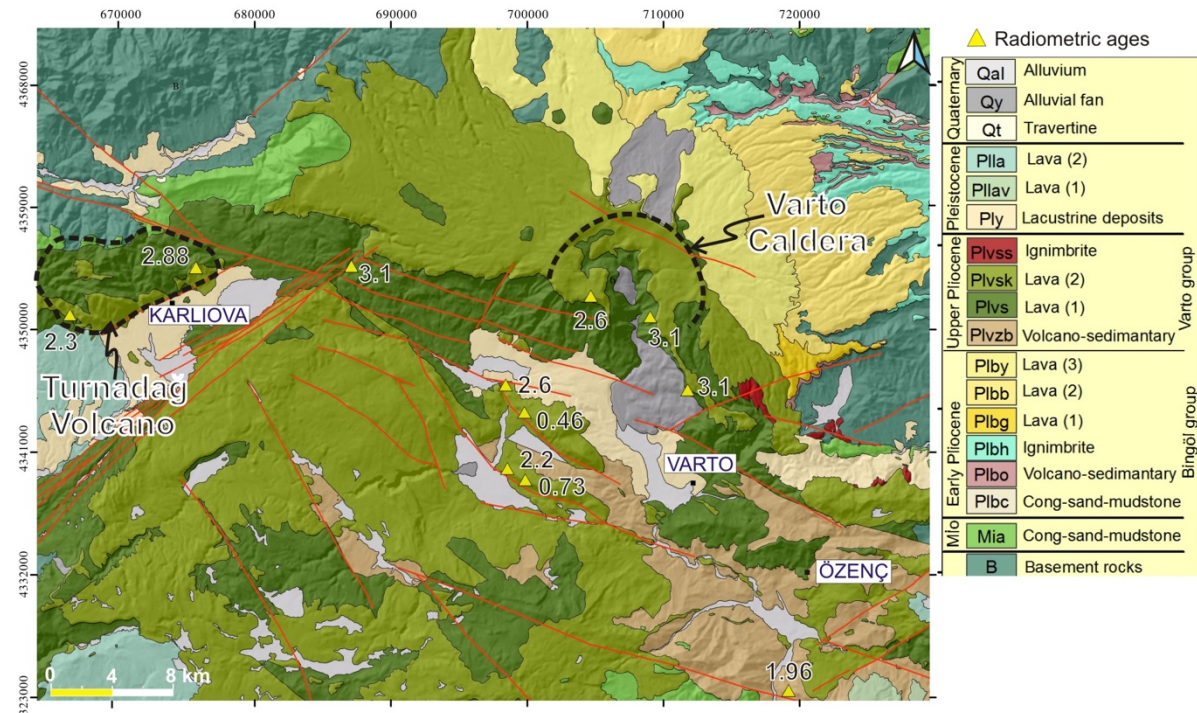
785
786
787
788

Figure Captions

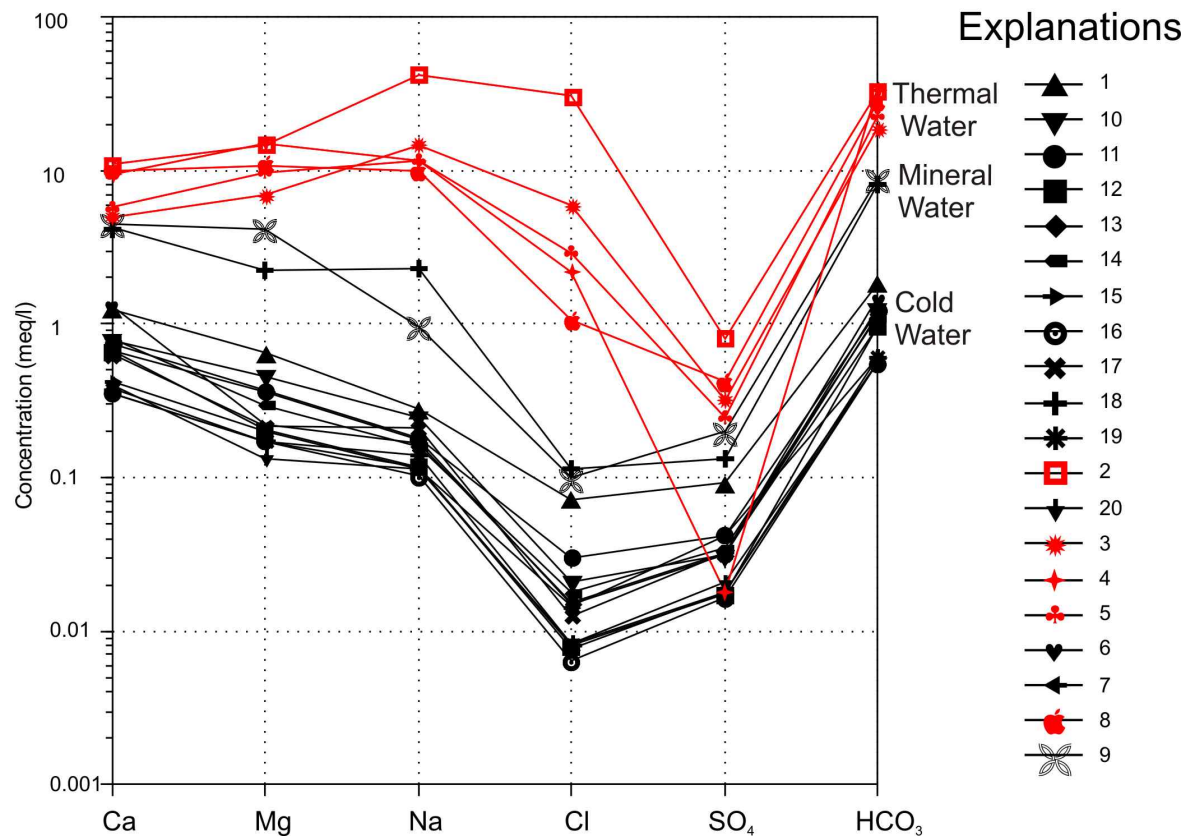
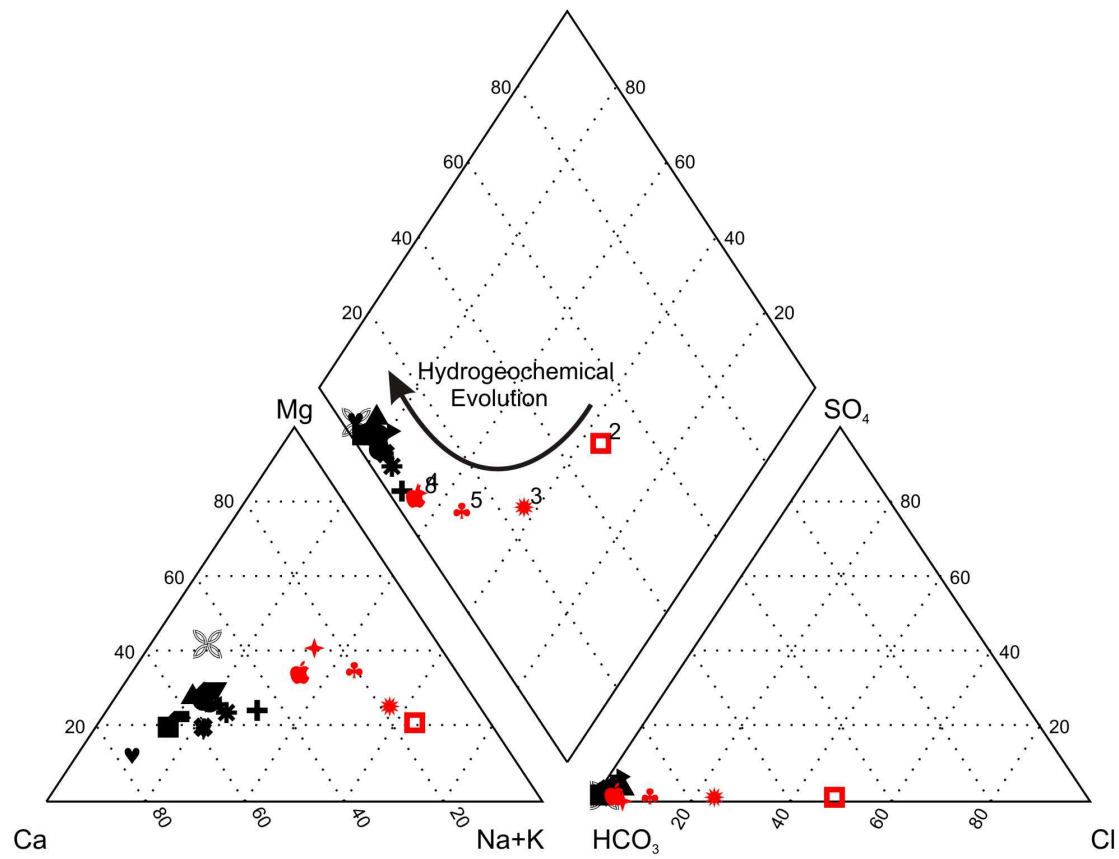


789
790
791
792
793
794
795
796

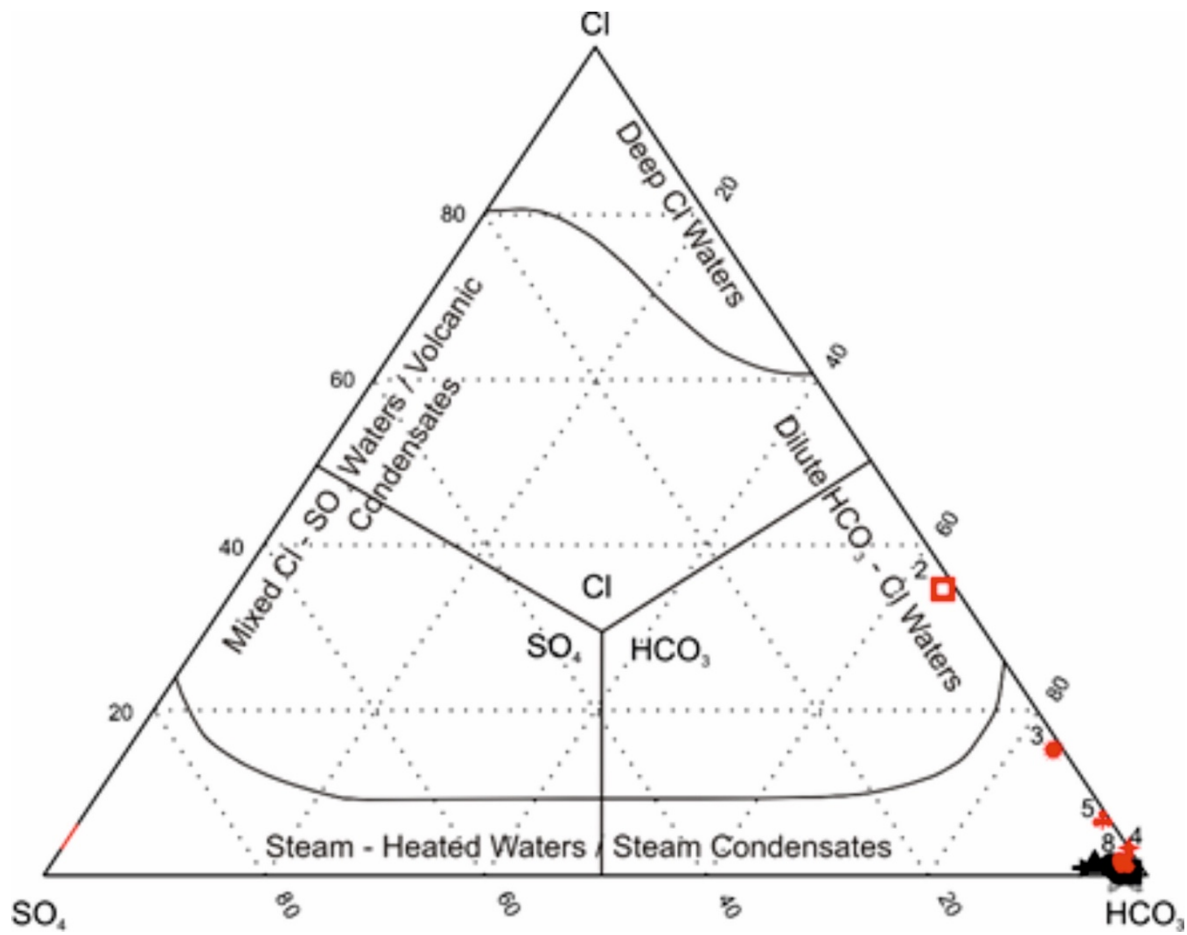
Figure 1. a) Regional map showing crustal deformation in the eastern Mediterranean and Anatolia (Armijo et al., 1999). NAFZ: North Anatolian Fault Zone, EAFZ: East Anatolian Fault Zone, BZCZ: Bitlis–Zagros Collision Zone, CF: Çaldıran Fault, VFZ: Varto Fault Zone, YS: Yedisu Fault, KTJ: Karlova Triple Junction; b) Shaded relief basis map showing locations of water sampling in the Varto region. The main faults and seismicity around the Karlova and Varto regions are modified from Herece (2008); Karaoğlu et al. (2017). Seismicity data is obtained from KOERI.



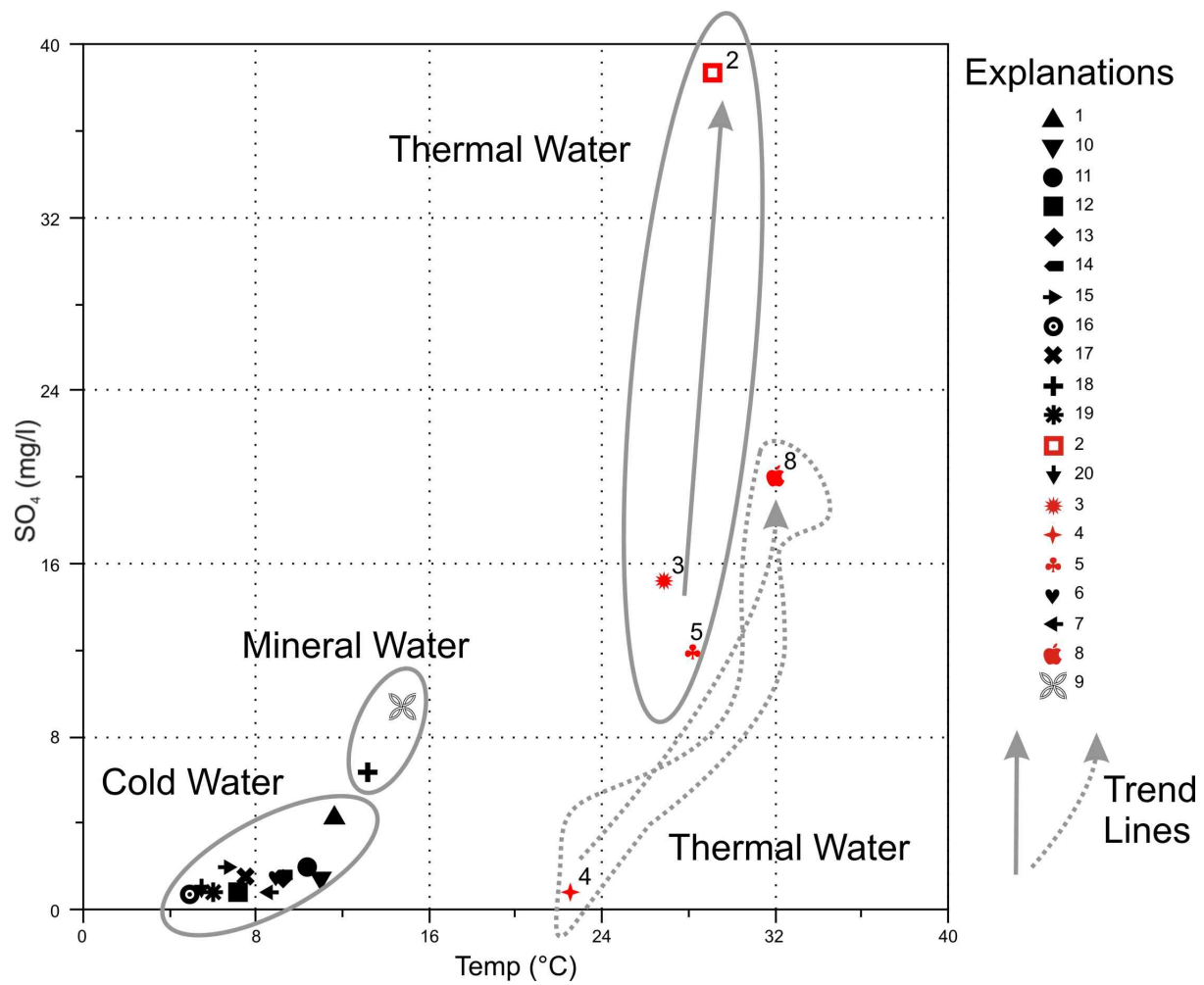
797
 798 **Figure 2.** Geological map showing the main faults and seismicity around the Karlıova and
 799 Varto regions. Radiometric ages are given in Ma. Active faults are modified from [Herece](#)
 800 [\(2008\)](#) and [Karaoğlu et al. \(2017\)](#). Thermal water signifies hot fluids that contain a variety and
 801 concentration of dissolved particles consistent with a thermal origin. The surface temperature
 802 of thermal water is higher than 20 °C. Mineral water means that which contains various
 803 minerals such as salts and sulfur compounds. These waters have temperatures lower than 20
 804 °C. Spring water is defined as natural water that was collected from underground sources.



805
 806 **Figure 3.** a) Map showing dominant stress orientations. b) Lower hemisphere equal area
 807 projections and striations on the main faults around the Varto-Karlıova region (data from
 808 Karaoğlu et al., 2017). Locations of the fluid measurement sites and kinematic stations are
 809 given in the map.



810
 811 **Figure 4.** a) Piper and b) Schoeller diagrams for the water resources in the study area. The red
 812 dots: thermal water, green dots: spring water, yellow dots: mineral water and blue dot: cold
 813 water.

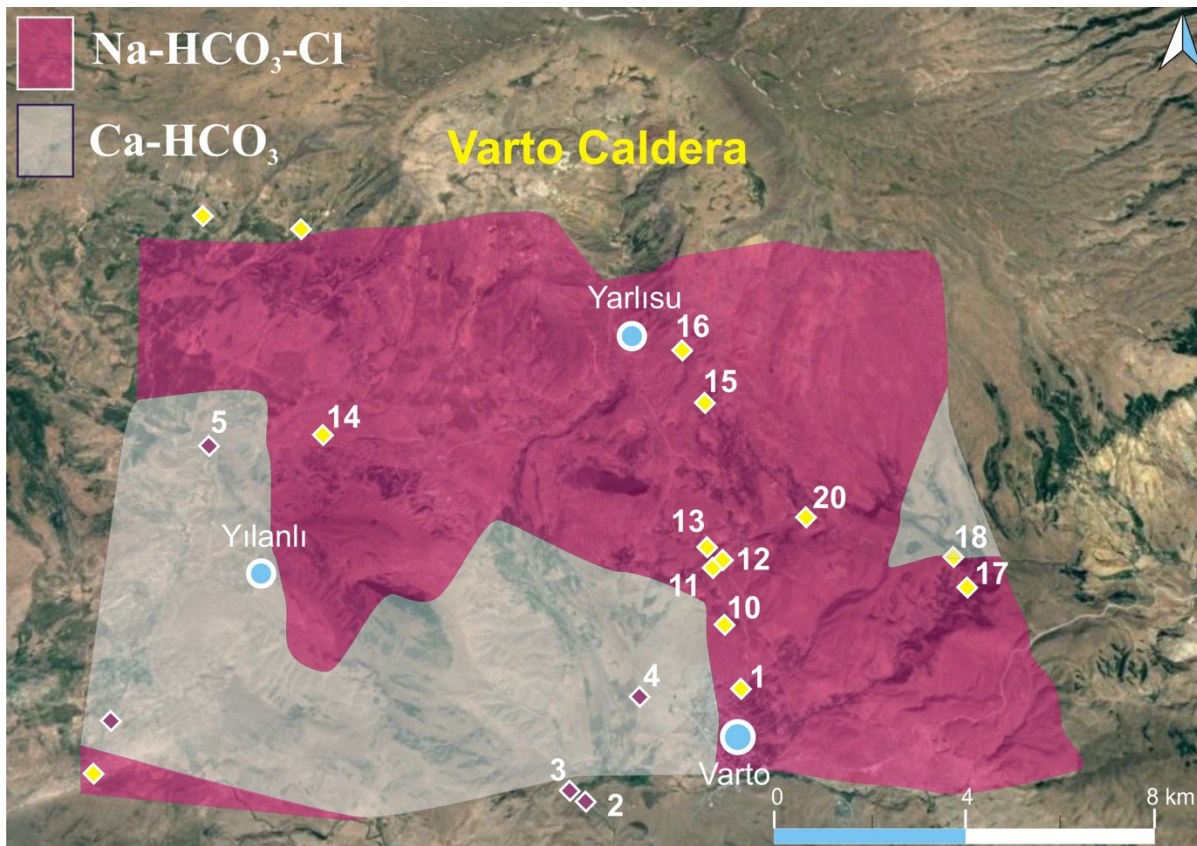


814

815 **Figure 5.** Cl-SO₄-HCO₃ Ternary diagram for the water resources in the study area.

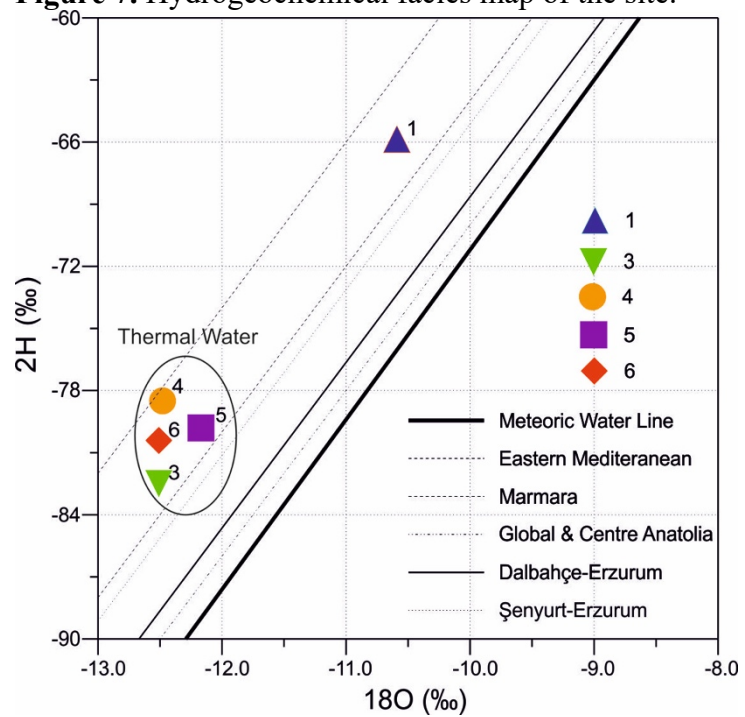
816

817 **Figure 6.** Scatter diagram and trend lines for the water resources in the study area.



818
819

Figure 7. Hydrogeochemical facies map of the site.



820
821

Figure 8. $\delta^{18}\text{O}$ versus δD diagram for the thermal waters in the study area.

822
823

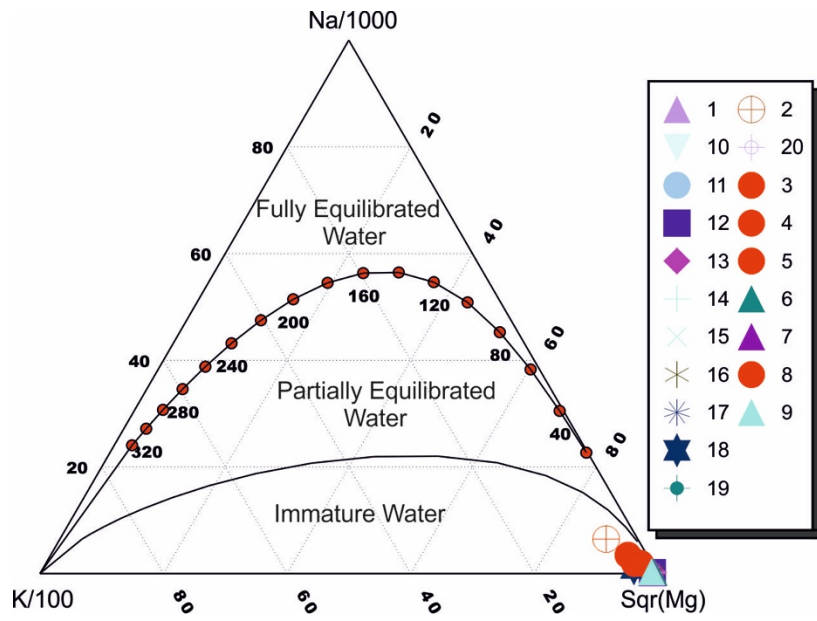
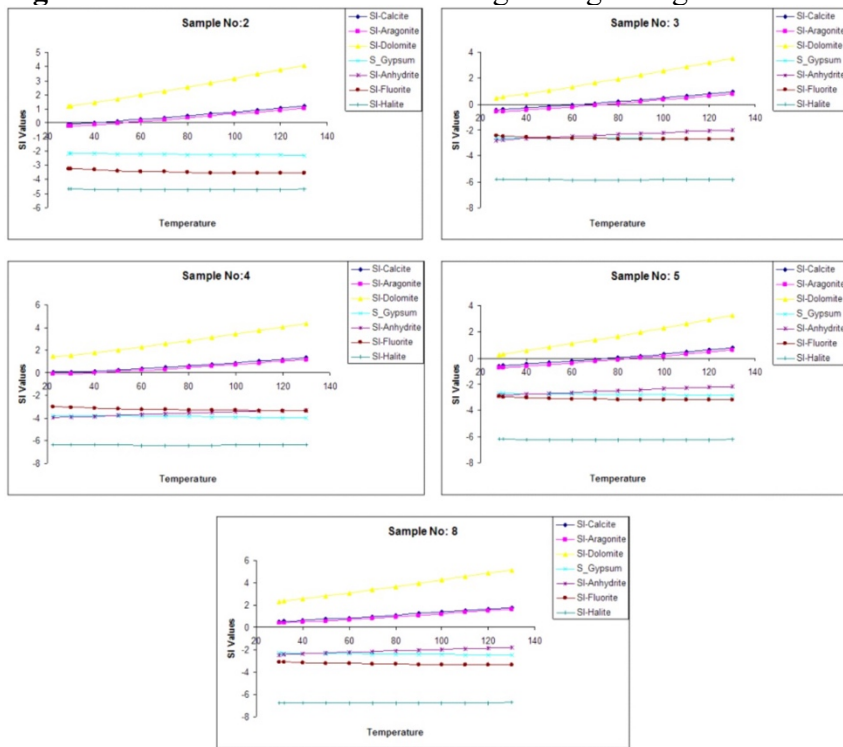
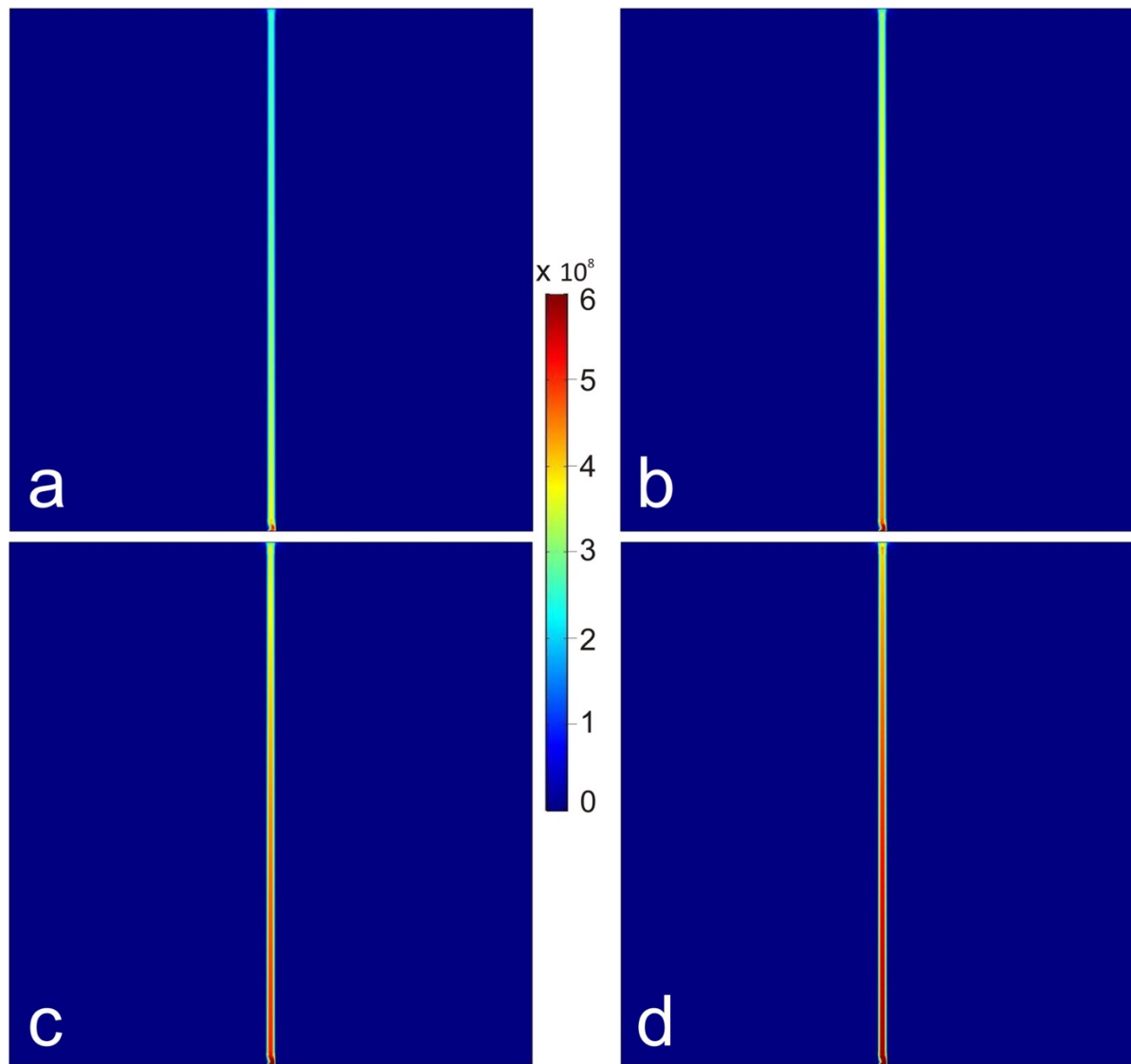


Figure 9. Thermal waters on Na-K-Mg Triangle diagram for the study area.



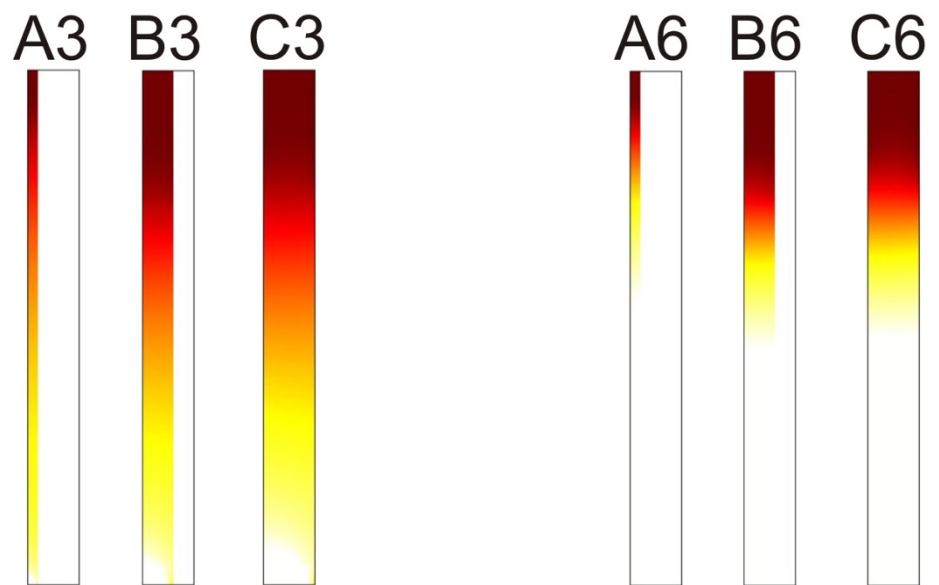
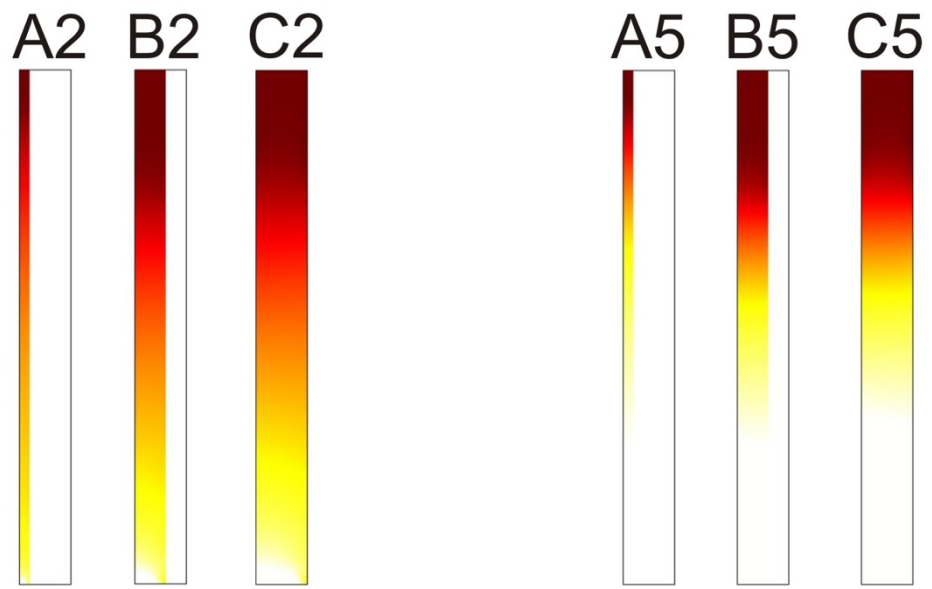
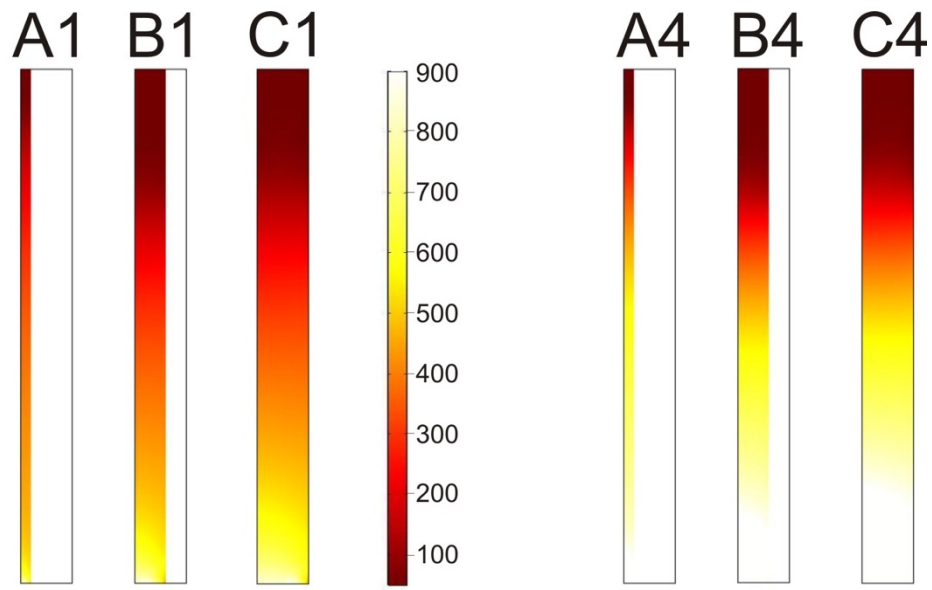
824
825
826

Figure 10. Changes in the selected mineral saturations of thermal waters at different temperatures in the Varto Geothermal Region.

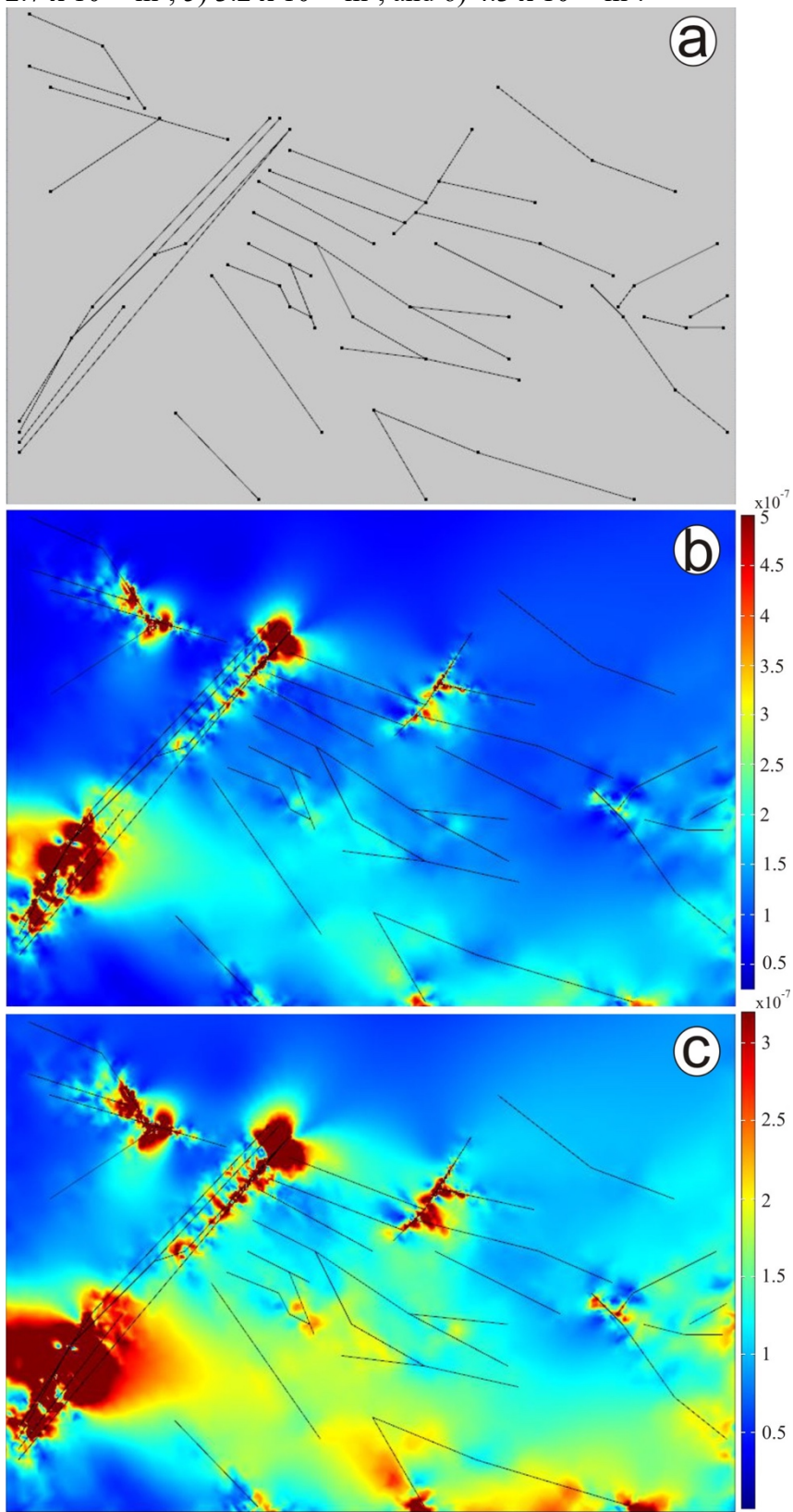


827
828
829
830
831
832
833
834

Figure 11. Fluid velocities as a function of permeability change. The fault in a) has a permeability of $1.0 \times 10^{-15} \text{ m}^2$ in part b) has a permeability of $2.1 \times 10^{-15} \text{ m}^2$, in part c) has a permeability of $3.2 \times 10^{-15} \text{ m}^2$ and in part d) has a permeability of $4.3 \times 10^{-15} \text{ m}^2$. In the model we also impose a temperature gradient from $900 \text{ }^\circ\text{C}$ at the base of the model to $25 \text{ }^\circ\text{C}$ at the surface. The maximum velocity field is found in the fault with the largest permeability as expected.

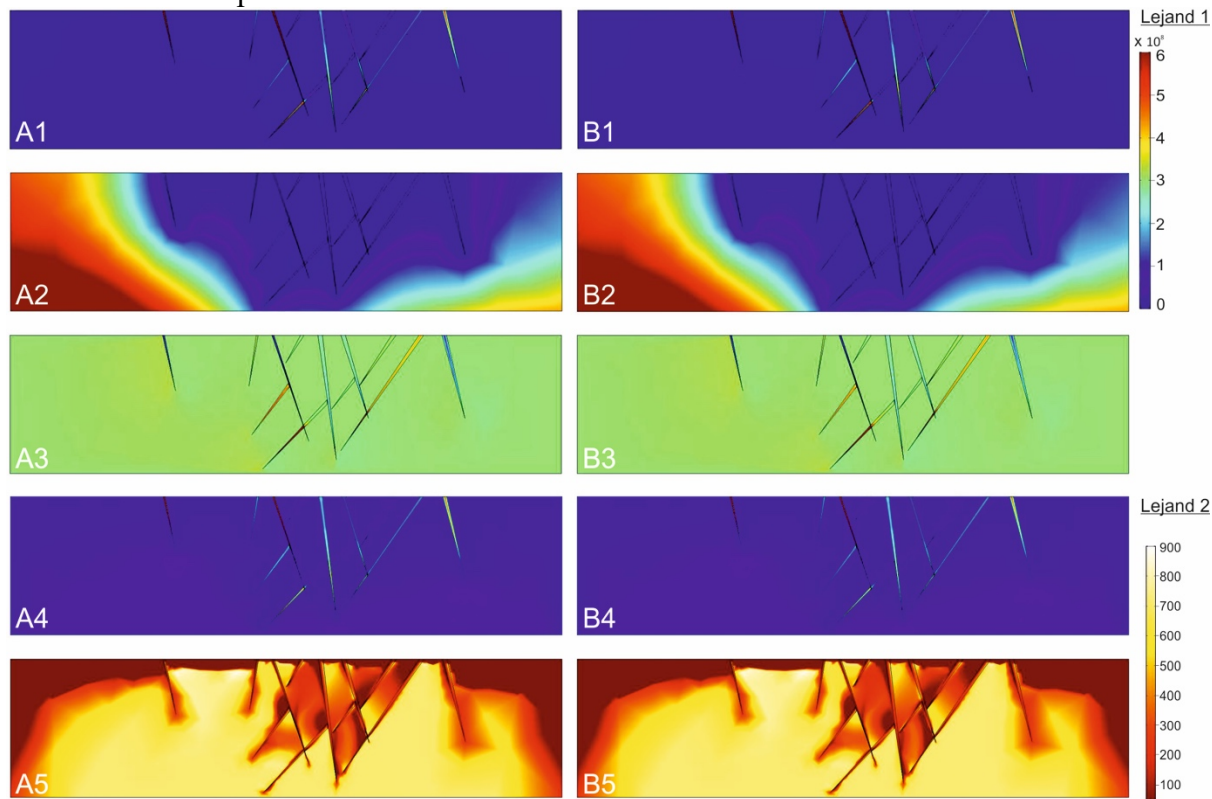


836 **Figure 12.** Fluid heat loss in the modelled fault as a function of fault width (L), and
837 permeability (k). The three different fault widths shown are 1 m, 5 m and 10 m. The six
838 different permeabilities (k) shown are 1) $1.0 \times 10^{-15} \text{ m}^2$, 2) $1.5 \times 10^{-15} \text{ m}^2$, 3) $2.1 \times 10^{-15} \text{ m}^2$ 4)
839 $2.7 \times 10^{-15} \text{ m}^2$, 5) $3.2 \times 10^{-15} \text{ m}^2$, and 6) $4.3 \times 10^{-15} \text{ m}^2$.

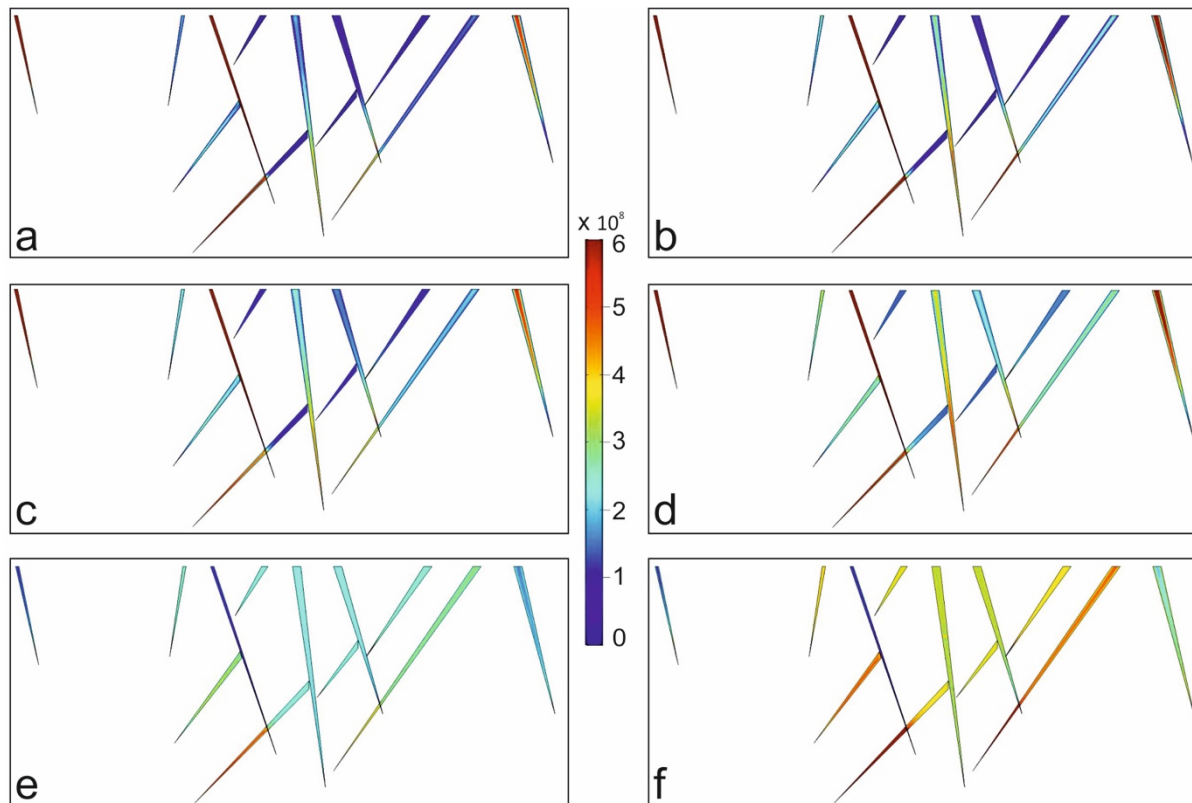


840 **Figure 13. a)** Surface view of the model setup where the lineations simulate faults based on
841 the geological setting along the Karlova Triple Junction region. The only loading in these
842

843 models is regional horizontal extension or compression. b) Modelled minimum principal
 844 compressive stresses induced from regional horizontal extension of 5 MPa. c) Modelled
 845 minimum principal compressive stresses induced regional horizontal compression of 5 MPa.
 846 NAFZ: North Anatolian Fault Zone, EAFZ: East Anatolian Fault Zone, VFZ: Varto Fault Zone,
 847 KTJ: Karliova Triple Junction.



848 **Figure 14.** A two dimensional vertical cross-section through a N-S striking profile of the
 849 faulted region around Varto caldera. The fault geometry is used as the model setup where each
 850 fault is assigned a different permeability. In all cases the top surface is unconstrained, whereas
 851 the x and lower y boundaries are fixed. The lower boundary of the model is assigned a starting
 852 temperature of 900 °C and the upper surface (free surface) is set at an atmospheric temperature
 853 of 25 °C.
 854



855 **Figure 15.** Fluid circulation in the fault zones around the Karlova region. A1) regional
 856 pressure at permeability $1 \times 10^{-15} \text{ m}^2$, B1) regional pressure at permeability $4.3 \times 10^{-15} \text{ m}^2$, A2)
 858 Fluid velocity within a fault of permeability $1 \times 10^{-15} \text{ m}^2$, B2) Fluid velocity within a fault of
 859 permeability $4.3 \times 10^{-15} \text{ m}^2$, displaying the total velocity field in both cases. A3) Fluid velocity
 860 within a fault of permeability $1 \times 10^{-15} \text{ m}^2$, B3) Fluid velocity within a fault of permeability 4.3
 861 $\times 10^{-15} \text{ m}^2$, displaying only the x direction (horizontal) flow in both cases. A4) fluid velocity
 862 within a fault of $1 \times 10^{-15} \text{ m}^2$, B4) fluid velocity within a fault of permeability $4.3 \times 10^{-15} \text{ m}^2$,
 863 displaying only the fluid velocity in the y direction (vertical) in both cases. A5) temperature
 864 field at permeability of $1 \times 10^{-15} \text{ m}^2$, B5) temperature field at permeability of $4.3 \times 10^{-15} \text{ m}^2$.
 865
 866